Rock Mechanics and Rock Engineering
https://doi.org/10.1007/s00603-025-04662-x

ORIGINAL PAPER

Mechanical Responses and Permeability Evolution in Porous Sandstones Under Cyclic Loading Conditions: Implications for Subsurface Hydrogen Storage

Ming Wen[1] · Nick Harpers[1,3] · Nathaniel Forbes Inskip[1] · Jim Buckman[2] · Kamaljit Singh[2] · Paul Miller[1] · Andreas Busch[1]

Received: 15 August 2024 / Accepted: 20 May 2025

Abstract

In underground hydrogen storage operations, reservoir rocks often experience periodic pore pressure fluctuations due to annual or more frequent gas extraction and injection cycles. These fluctuations subject the reservoir rocks to cyclic effective stress changes, causing their mechanical and transport behaviors to differ from those under static conditions. However, understanding how porous rocks react to cyclic loading conditions is still limited. To bridge previous research gaps, cyclic loading tests were conducted on Castlegate and St Bees Sandstone, with applied stress amplitudes ranging from 70 to 90% of their monotonic peak strength. This experimental approach was designed to replicate the in situ stress conditions experienced by reservoir rocks during gas operations. Concurrently, we utilised the steady-state method to measure permeability changes under cyclic loading. By comparing the micro-CT features of the sandstones before and after cyclic loading tests, we quantitatively analysed the microscopic mechanisms driving these alterations in sandstone samples. Our results show that under cyclic loading conditions, the inelastic axial strain and Young's Modulus initially increase for both sandstones, with the most significant changes occurring within the 1st cycle, followed by a trend towards stability. Permeability decreases with increasing stress and loading cycles. For the Castlegate Sandstone, elevated confining pressure intensified permeability loss, while in St Bees Sandstone, high confining pressure resulted in less permeability loss compared to low confining pressure, which was related to shear band development. Microstructural analysis showed grain movement, rotation, and rearrangement in Castlegate Sandstone under external forces, leading to pore/throat compression and reduced porosity/permeability. In contrast, St Bees Sandstone microstructure changes under low stress involved grain cracking from shear dilatancy, increasing porosity but blocking throats, complicating pore structure, then reducing permeability. Under high confining pressure, the strength of St Bees Sandstone rose without sufficient differential stress for shear dilatancy. Decreased permeability and pore volume were linked to compaction-dominated deformation.

Highlights

- Castlegate and St Bees Sandstones exhibit prominent hysteresis loops under cyclic loading, with maximum inelastic strain and stiffness variations during the 1st loading cycle.
- Castlegate Sandstone experiences more pronounced permeability loss under elevated confining pressures due to pore/throat compaction driven by grain rearrangement.
- St Bees Sandstone shows complex permeability changes, with shear-induced grain cracking at lower confining pressures increasing porosity but reducing permeability by blocking pore throats.
- Variations in mechanical and permeability responses are closely linked to grain size distribution and morphology differences between the two sandstones.

✉ Ming Wen
mw107@hw.ac.uk

[1] The Lyell Centre, Heriot-Watt University, Edinburgh EH14 4AS, Scotland, UK

[2] Institute of GeoEnergy Engineering, Heriot-Watt University, Edinburgh EH14 4AS, Scotland, UK

[3] Applied Structural Geology Teaching and Research Unit, RWTH Aachen University, 52064 Aachen, Germany

Published online: 16 June 2025

Keywords Underground hydrogen storage · Porous sandstones · Cyclic loading · Permeability evolution · Micro-CT

1 Introduction

Renewable energies are becoming increasingly important in replacing fossil fuels as the main source of energy worldwide. They relate to small amounts of greenhouse gases emitted to the atmosphere and therefore support global ambitions towards achieving net zero (Canadell et al. 2023; Engeland et al. 2017). However, the production of energy from some renewable sources is intermittent and/or non-constant (e.g. wind power and solar photovoltaic). This can lead to a mismatch between energy supply and demand. Therefore, the strategic implementation of underground gas storage, including the cyclic storage of hydrogen and natural gas, emerges as an effective solution to reconcile this imbalance (Carden and Paterson 1979; Lund and Salgi 2009; McPherson et al. 2018). While natural gas is a primary source of energy, typically stored underground during summer months on the northern hemisphere, underground hydrogen storage (UHS) is currently considered as a secondary source of energy produced during times of overproduction from renewables. The hydrogen for underground storage is usually produced by electrolysing water with excess renewable energy or through processing fossil fuels. This produced hydrogen is stored in depleted oil and gas fields, salt caverns, or aquifers. Once there is a surge in energy demand or an interruption in the supply of renewable energy, the stored hydrogen can be quickly released and used to produce electricity to meet immediate needs (Zivar et al. 2021). It not only ensures a reliable and continuous supply of energy, optimizing the utilization of renewable resources, but also significantly reduces our reliance on traditional carbon-intensive energy sources, bringing us closer to the realization of a sustainable and balanced energy future.

Underground hydrogen storage can be achieved by utilising salt caverns or porous media, such as saline aquifers or depleted hydrocarbon reservoirs (Lankof and Tarkowski 2020; Reitenbach et al. 2015; Zivar et al. 2021). Compared to salt cavern storage, gas storage in porous sandstone reservoirs offer some advantages, including high storage capacity and the capability for long-term storage (due to their high chemical inertness) (Heinemann et al. 2021). These attributes make porous sandstones a feasible option for enhancing energy security and sustainability. However, unlocking this potential relies on a deep and comprehensive understanding of the physical properties of sandstones under in situ conditions.

Previous studies have shown that annual or more frequent gas production and injection processes alter the pore pressure within reservoir rocks. This cycling of pore pressure leads to periodic fluctuations in effective stress. Such periodic stress states are considered key factors influencing the mechanical and transport properties of reservoir rocks (Mortazavi and Atapour 2018; Rafieepour et al. 2017; Rafieepour et al. 2021). Several studies suggested that cyclic loading can result in a decrease in the stiffness of sandstone and an increase in Poisson's ratio, which can be associated with crack evolution (Huang et al. 2018; Zhou et al. 2017). The propagation of cracks plays an important role in altering the transport properties of rocks (Popp et al. 2001; Zhao et al. 2019). However, it is also argued that under cyclic loading and unloading, the closure of microcracks and pores leads to an increase in the strength of sandstone (Taheri et al. 2016), accompanied by a decrease in porosity and permeability (Dong et al. 2010). This lack of consensus not only highlights the complexity of the issues but also indicates that the behaviour of different sandstones under stress can vary greatly. While prior studies provide some insights into the response of reservoir rock transport properties to cyclic stress, there remains a gap in our understanding of how cyclic loading affects the transport properties of reservoir rocks at the microscopic scale (Dong et al. 2010; Wang et al. 2017). Specifically, the microscopic mechanisms behind the observed changes in permeability remain poorly understood. Furthermore, a significant limitation of previous studies is the stress ranges used in experiments, which often fail to accurately reflect the in situ stress conditions encountered in underground environments designated for hydrogen storage (Heinemann et al. 2021; Kumar et al. 2023). This discrepancy raises doubts about the applicability of these research findings to real-world scenarios. Filling these knowledge gaps and overcoming these research limitations will not only improve the optimization of underground hydrogen storage strategies but also strengthen our ability to predict and mitigate the risks associated with such efforts.

In this study, we employed a multi-scale workflow, initiating high-resolution micro-CT imaging of the microstructures of two sandstone samples before the experiments and reconstructing the pore/grain geometries. Subsequently, cyclic loading tests were performed to simulate the in situ stress experienced by reservoir rocks due to gas injection/extraction. Simultaneously, we employed a steady-state method to measure the permeability at critical stress steps and analysed the evolution of rock mechanics and transport properties under cyclic loading conditions. By comparing the micro-CT features of the sandstones before and after cyclic loading tests, the microscopic mechanisms behind these changes in sandstone samples were quantitatively analysed. This study investigates how stress cycling during underground hydrogen storage affects the mechanical and transport properties of porous sandstone, and aims to understand the underlying

microscopic mechanisms, providing guidance for the optimal operation of underground hydrogen storage reservoirs.

2 Materials and Methods

2.1 Materials

The samples used in this study are Castlegate and St Bees Sandstone. The Castlegate Sandstone originates from Utah, USA. It is a yellow sandstone that developed in the Upper Cretaceous Mesaverde Group. It is primarily composed of quartz, typically constituting over 90% of its composition, with minor amounts of feldspar and clay minerals (< 5%) (Miall and Arush 2001). The grain size varies from medium to coarse, with an average grain size of 0.2 mm, featuring good sorting, high roundness, and strong homogeneity. It possesses remarkably high porosity and permeability, with porosity exceeding 20% and permeability typically on the order of 10^{-13} m^2. This sandstone is generally considered an optimal reservoir analogue for experimental research. (Kibikas and Bauer 2021; Mortazavi and Atapour 2018). The St Bees Sandstone is a Permian red sandstone and primarily distributed in Cumbria, UK. This sandstone is mainly composed of quartz and feldspar, with a notably high quartz content exceeding 75%. Feldspar follows, constituting 10–20% of the total volume (Hawkins and McConnell 1991). The grain size typically ranges from fine to medium, with an average grain size of ~ 0.15 mm, demonstrating favourable sorting and a subangular to subrounded shape. It exhibits good porosity and permeability and is considered an important aquifer in Cumbria, England (Medici et al. 2018). In this study, all samples were drilled perpendicular to bedding from larger blocks collected from outcrops, and both ends of the samples were ground flat and perpendicular to the sample axis using grinding papers to ensure uniform loading distribution during the tests. After drilling, these samples were dried in an oven at 70 °C for 24 h for the experimental testing. The initial porosity of all samples was determined by combining Archimedes' principle with CT image analysis. Basic physical parameters of the porous sandstone sample and testing conditions are shown in Table 1.

2.2 Experimental Apparatus

The cyclic loading experiments were performed using the Harpers THMC Flow Bench (Harpers et al. 2023). This system is capable of reproducing in situ stress conditions and performing coupled temperature–hydraulic–mechanical–chemical experiments on small rock samples with dimensions of 10 mm in diameter by 20 mm in length. The confining and pore pressures are up to 20 MPa, axial stress up to 300 MPa and temperature up to 90 °C. The experimental system consists of four identical high-pressure triaxial cells that can be operated in parallel or individually. The four cells are controlled by three sets of independent pressurization systems for confining pressure, axial stress, and pore fluid pressure, as shown in Fig. 1. Axial load is provided through high pressure nitrogen and controlled by a spindle pump. The gas pressurises an axial load intensifier

Table 1 List of samples, experiments, test conditions, and key data

Sample number	Diameter (mm)	Length (mm)	P_c(MPa)	P_p(MPa)	Q(MPa)	Cycles	Inelastic strain (%)	Porosity (%)	Permeability (m^2)[a]
CG-1	9.19	19.90	10.5	1	25–42	0	0	18.8	3.26×10^{-13}
						5	0.43	18.5	2.36×10^{-13}
						20	0.62	18.3	2.23×10^{-13}
CG-2	9.19	19.88	10.5	1	0–42	0	0	18.5	3.88×10^{-13}
						5	0.63	18.3	2.51×10^{-13}
CG-3	9.21	19.81	19.5	1	0–42	0	0	18.4	3.99×10^{-13}
						5	0.34	17.9	2.36×10^{-13}
ST-1	9.21	19.61	10.5	1	25–42	0	0	20.1	2.00×10^{-13}
						5	0.69	20.4	7.83×10^{-13}
						20	0.86	20.6	7.48×10^{-13}
ST-2	9.18	19.74	10.5	1	0–42	0	0	20.1	2.59×10^{-13}
						5	0.78	20.4	5.71×10^{-14}
ST-3	9.19	19.70	19.5	1	0–42	0	0	20.1	2.31×10^{-13}
						5	0.48	20.1	1.48×10^{-14}

P_c = confining pressure; P_p = pore pressure; Q ($\sigma_1^{eff} - \sigma_3^{eff}$) = effective differential stress

[a]the permeability values for CG-1 and ST-1 were measured under low-stress conditions, i.e. during unloading after in situ stress, whereas those for CG-2, CG-3, ST-2, and ST-3 were obtained under conditions of zero differential stress

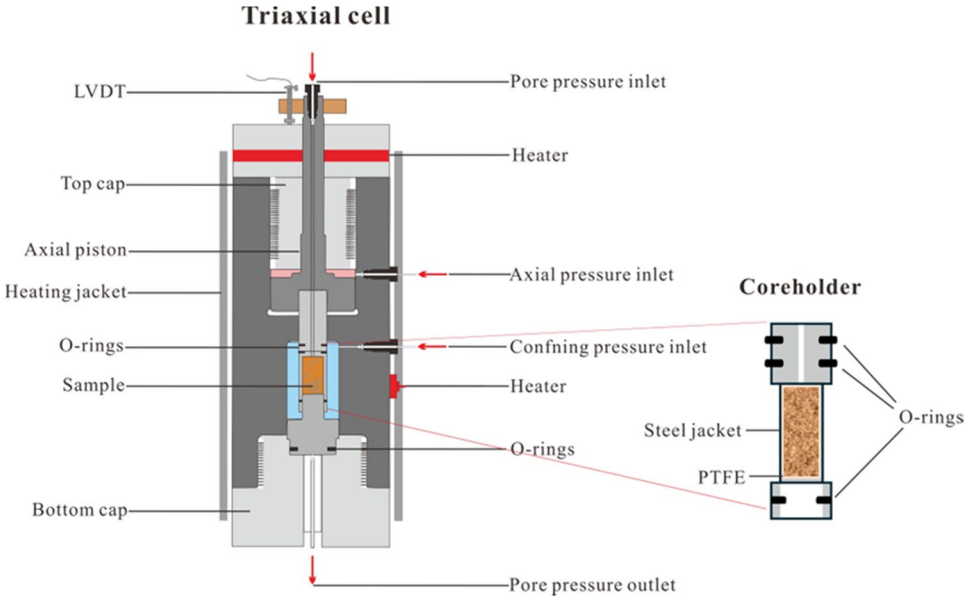

Fig. 1 Schematic diagram of high-pressure triaxial cells of the Harpers THMC Flow Bench (Harpers et al. 2023)

that amplifies the provided gas pressure by a factor of 15. Two high-pressure syringe pumps are responsible for supporting the system with confining pressure (Teledyne ISCO Model 260D, USA)) and pore pressure (Teledyne ISCO Model 500D, USA), respectively. The operating principles and processes of Harpers THMC Flow Bench are described in detail by Harpers et al. (2023). In this study, the sandstone samples are coated with PTFE (Polytetrafluoroethylene) to seal the space between the sample and the steel jacket with a thickness of 0.064 mm, preventing fluid bypass. In addition, each cell is equipped with a linear variable differential transducer (LVDT; ± 1 mm range; 1 µm accuracy RDP Electronics Ltd, UK) on the top cap to measure the axial deformation of the samples.

2.3 Experimental Procedure

2.3.1 Cyclic Loading and Permeability Test Under In Situ Stress Conditions

Previous studies have shown that the optimum depth for subsurface hydrogen storage is 1100 m, and that depths greater than 3700 m are theoretically unsuitable for long-term, large-scale subsurface hydrogen storage (Iglauer 2022). Considering the suitable burial depth for hydrogen storage reservoir and the apparent response of the reservoir rocks to cyclic stresses, this paper simulated the extreme conditions of full pore pressure cycling under in situ reservoir stresses of ~ 2000 m depth. We assumed that the maximum in situ stress (σ_1) of the reservoir is in the vertical direction. Its magnitude is equivalent to the integral of rock density from the surface to the target depth z (Zoback 2010):

$$\sigma_1 = \int_0^z \rho(z) g dz \approx \overline{\rho} g z \tag{1}$$

The bulk density of sandstone is generally between 2.0 and 2.6 g/cm^3. For calculation convenience, we approximate the density of sandstone to be 2.5 g/cm^3. Therefore, the approximate magnitude of the in situ vertical stress (σ_1) is 50 MPa. Additionally, assuming that the minimum horizontal stress (σ_3) is half the vertical stress (σ_1), and the pore pressure is equal to the hydrostatic pressure (Fjaer et al. 2008; Zoback 2010), then the in situ minimum horizontal stress (σ_3) and pore pressure (P_p) at the end of injection are, respectively, 25 MPa and 20 MPa. This means that the differential stress Q ($\sigma_1^{eff} - \sigma_3^{eff}$) is 25 MPa after full injection. When the gas is completely extracted and the pore pressure reaches 0.1 MPa, the effective stress σ_1^{eff} is restored to 50 MPa, while the change in σ_3^{eff} can be roughly estimated using a uniaxial strain model (Pijnenburg et al. 2018):

$$\Delta\sigma_3^{eff} = \alpha \Delta P_p \left(\frac{-\nu}{1-\nu} \right) \tag{2}$$

Assuming the Poisson's ratio (ν) of porous sandstone is 0.15 ± 0.05 (Hettema et al. 2000; Pijnenburg et al. 2018), then σ_3^{eff} is estimated to increase to 8.5 MPa during depletion, and σ_1^{eff} increases 50 MPa. Therefore, the range of differential stress Q ($\sigma_1^{eff} - \sigma_3^{eff}$) changes during the cyclic loading process from 25 MPa (full injection) to 42 MPa (depletion). The maximum confining pressure of The Harpers THMC Flow Bench can only reach 20 MPa. Therefore, in this experiment, we achieved differential stress cycles by setting the confining pressure

to 10.5 MPa, the pore pressure to 1 MPa, and cyclically varied the axial pressure from 35.5 to 52.5 MPa. It should be noted that previous field case studies and numerical feasibility analyses on underground hydrogen storage (UHS) in porous media have typically employed relatively modest reductions in pore pressure, generally limited to within 10 MPa, to ensure borehole stability and maintain adequate reservoir flow performance (Lysyy et al. 2021; Pfeiffer and Bauer 2015). In contrast, the present study adopts a pore pressure reduction of 20 MPa during reservoir depletion. While this may appear extreme from an operational perspective, such stress paths exceeding anticipated field conditions are routinely employed at laboratory scale to establish mechanical failure envelopes for rock specimens. By imposing this elevated pore pressure drop, the experimental conditions effectively induce deformation and damage mechanisms pertinent to UHS scenarios. Consequently, the application of elevated pore pressure reduction serves to actively induce deformation and damage mechanisms analogous to those potentially occurring during UHS operations. This approach provides critical safety margins when extrapolating rock mechanical responses to actual subsurface hydrogen storage conditions.

The experimental steps are as follows: all sandstone samples were coated with PTFE, placed into the coreholders, and subjected to CT scanning. Subsequently, the coreholders were positioned in the cells, assembled into position, and vacuumed for 15 min. Initially, the syringe pump applied a confining pressure of 10.5 MPa to the samples at an average loading rate of 0.06 MPa/s until the desired value was reached. Simultaneously, the axial pressure was increased to a value equal to the confining pressure to keep the sample at hydrostatic pressure (Q=0). Subsequently, deionized water was injected into the core holders until the pore pressure reached 1 MPa, with a loading rate maintained at 0.05 MPa/s. After the whole system was equilibrated for 10 min, axial compression was loaded at an average loading rate of 0.1 MPa/s until the differential stress increased to 25 MPa. In this study, axial stress was increased while maintaining a constant confining pressure. This was primarily due to the relatively small stress range used in the experiments. The main focus is on examining the impact of increased differential stress, whereas the increase in horizontal effective stress was considered secondary (Pijnenburg et al. 2018).

The steady-state method is employed to measure rock permeability. The permeability of the rock sample was calculated using Darcy's law after a steady pressure or flow rate was observed for several minutes (Zhu and Wong 1997):

$$k = \frac{q\mu L}{(\Delta p)A} \tag{3}$$

where q, μ, Δp are the fluid velocity ($m^3.s^{-1}$), viscosity (Pa.s), and pressure difference between the inlet and outlet (Pa), while A and L are the sample cross-sectional area (m^2) and length (m), respectively. Subsequently, samples were continuously loaded at the same rate until the differential stress reached a maximum of 42 MPa, and the permeability at that stress point was measured again. Following the permeability test, the samples were unloaded at the same rate until the differential stress reached 25 MPa, and the permeability of the samples was measured again. The experiments were repeated in the same manner until after the 5th cycle and the core holders were removed for CT scanning. Then, the experiments were continued until the 20th cycle was completed, after which the sample was removed from the core holder, dried, and subjected to CT scanning again. It should be noted that this study measured only the vertical permeability, which represents the permeability in the direction of the maximum principal stress and did not provide the changes in permeability in the direction of the minimum principal stress, i.e., the radial permeability. See Fig. 2a for the schematic diagram of experimental processes.

2.3.2 Cyclic Loading and Permeability Test Under Fully Cyclic Loading Conditions

To investigate the permeability evolution with stress and the inelastic strain accumulation with each loading cycle, we performed full cyclic differential stress experiments on Castlegate and St Bees Sandstone using The Harpers THMC Flow Bench System. In this study, the pore pressure was maintained constant at 1 MPa. Cyclic axial stress was applied, varying the differential stress from 0 to 42 MPa over 5 cycles. For comparative analysis, two confining pressures, 10.5 and 19.5 MPa, were applied to study the effects of confining pressure on rock properties. The permeability of the samples was measured using the steady-state method, and axial strain was recorded with LVDTs. The experimental procedure is roughly the same as the in situ stress cyclic loading experiment. The difference is that the steady-state method is used to measure the rock permeability at differential stress steps of 0, 10.5, 21, 31.5, and 42 MPa in this experiment (Fig. 2b).

2.4 Microstructural Characterization

X-ray micro-CT scanning of cylindrical samples was performed to characterise the microstructure of the material before and after permeability and mechanical tests. All CT experiments were performed with a high-resolution EASYTOM µCT scanning device at Heriot-Watt University (RX-Solutions, France). The scanner operates at a voltage of 150 kV and 500 µA. Each scan took 120–150 min and generated 3800–4400 projections with a voxel size of 7.71 µm. The principle of CT scanning involves the emission of an electron beam from a cathode, which upon

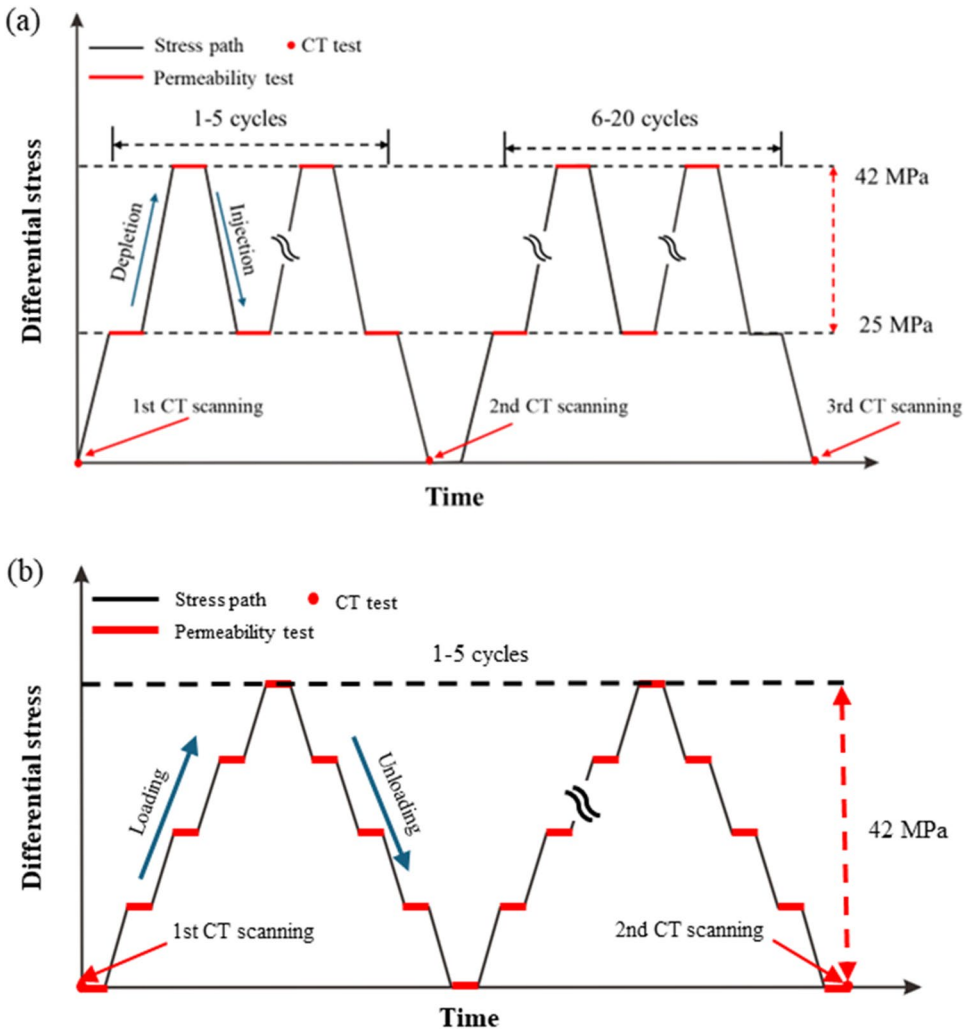

Fig. 2 Schematic diagram of experimental procedures. **a** Cyclic loading and permeability test under in situ stress conditions. **b** Permeability test under fully cyclic loading conditions

striking a tungsten anode target, produces a broad spectrum of X-rays. These X-rays penetrate the rotating sandstone, and detectors capture two-dimensional projection images at various angles. Subsequently, these projection images were reconstructed into a three-dimensional image using the RX-Solutions three-dimensional analysis software. The three-dimensional reconstructed images of Castlegate Sandstone and St Bees Sandstone before and after the cyclic loading test are illustrated in Fig. 3.

After the reconstruction, the scanned sandstone images were processed and analyzed using Avizo 2020 (Thermo Fisher scientific, USA), a commercial 3D image processing and analysis software. Noise was removed through median filtering, and non-local means denoising. Subsequently, a

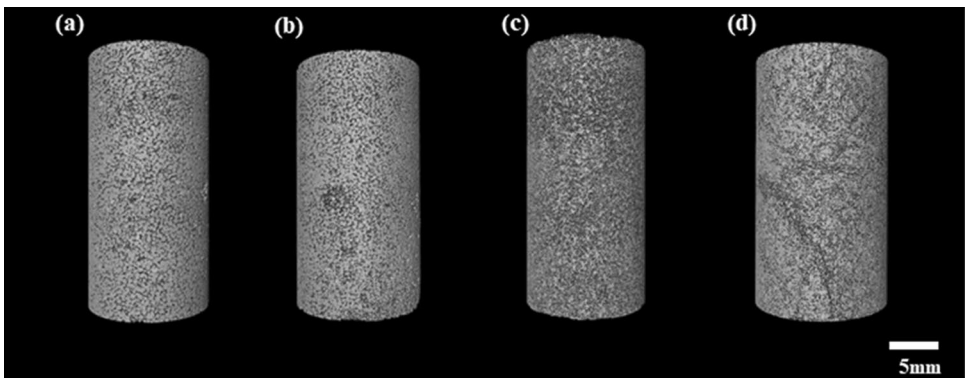

Fig. 3 The three-dimensional structure of Castlegate (CG) and St Bees (ST) Sandstone. **a** CG-1 before the test; **b** CG-1 after 30 loading cycles; **c** ST-1 before the test; and **d** ST-1 after 30 loading cycle

watershed algorithm was applied to identify the optimal thresholds for pore segmentation. Following pore segmentation, connected pores were processed to construct Pore Network Models (PNM) (Dong and Blunt 2009). To characterise the alterations in transport properties of sandstone, we conducted an in-depth analysis of pore structure parameters such as tortuosity, pore/throat size, and coordination number. Coordination number in a pore network model (PNM) serves as an index describing the number of throats connecting a pore to its neighboring pores (Desbois et al. 2016). It is a critical topological parameter that illustrates the connectivity and complexity within a porous sandstone, directly impacting the transport characteristics of reservoir rocks. A higher coordination number indicates better pore connectivity, which is beneficial for fluid flow. Tortuosity τ (-) a dimensionless value, describes the complexity and meandering nature of fluid pathways L (m) through porous media relative to a straight-line distance L_0 (m). It is typically defined as the ratio of the actual path length of a fluid through a porous medium to the straight-line distance between two points within that medium (Doyen 1988; Lindquist et al. 2000):

$$\tau = \frac{L}{L_0} \tag{4}$$

Tortuosity typically exceeds 1 since the actual flow path is longer than the straight-line distance (Gong et al. 2020). Moreover, grain analysis including grain size, orientation, and grain morphology analyses were conducted on the sandstone before and after experiments to analyse the micro-mechanisms of mechanical and transport property variations under cyclic loading conditions. For grain analysis, a logical algorithm was employed to segment the sandstone grains further. Once the sandstone grains were labelled, morphological attributes such as size, orientation, and shape were characterised by extracting parameters including Length3D, Width3D, EqDiameter, OrientationPhi, OrientationTheta and Sphericity. In the case of CT imaging, Length3D and Width3D, respectively, represent the maximum and minimum of the grain's Feret diameter, which is defined as the distance between two parallel lines, which are tangent to the object contour and perpendicular to the specified direction (Kong et al. 2018). The aspect ratio is defined as the ratio of the Length3D to Width3D. OrientationPhi and OrientationTheta represent the angles of the grains in φ [0, + 90º] and θ [-180,180º] directions, as illustrated in Fig. 4. These angles are determined via the inertia moment calculation (Herlinger and Vidal 2022).

The equivalent diameter EqD of a grain represents the diameter of a sphere with the same volume V_{grain} (m^3) as the grain, calculated by the following formula:

$$EqD = \sqrt[3]{\frac{6V_{grain}}{\pi}} \tag{5}$$

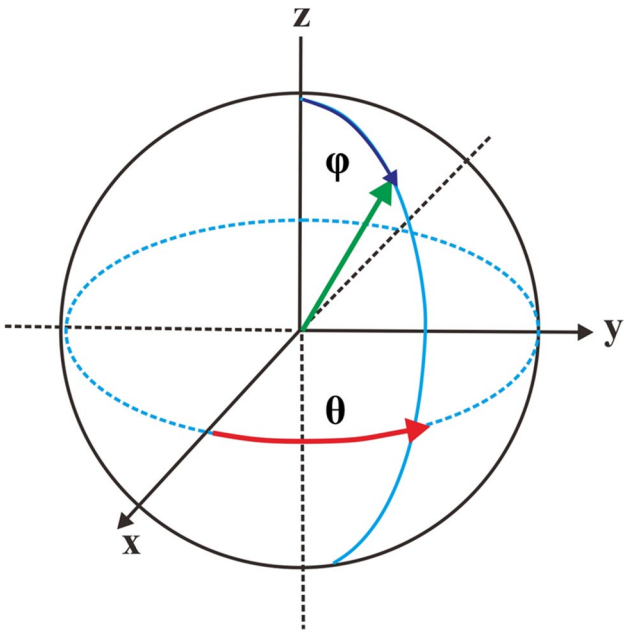

Fig. 4 Schematic diagram of Phi (φ) and Theta (θ) in polar coordinates on the x, y, and z axes

Additionally, sphericity indicates the degree to which a grain approaches a perfect sphere, calculated by the following formula:

$$Sphericity = \frac{\pi^{\frac{1}{3}} 6V_{grain}^{\frac{2}{3}}}{A_{surf}} \tag{6}$$

where A_{surf} is the surface area of the grain. Sphericity varies between 0 and 1; a higher sphericity indicates better grain roundness (Kong et al. 2019). A Schematic diagram of the overall process of sandstone CT processing is shown in Fig. 5.

3 Results

3.1 Mechanical Responses of Sandstones Under Cyclic Loading Conditions

In Fig. 6, we show cyclic differential stress versus axial strain of Castlegate and St Bees Sandstone under various stress conditions. Under in situ stress conditions, the two types of porous sandstones exhibited nonlinear, upwardly concave stress–strain behaviour during initial loading, associated with the closure of original microcracks (Peng et al. 2015; Zhang and Tang 2020). With increasing stress, this shifts to a relatively stiff, nearly linear elastic deformation zone. As the differential stress increases to 38 MPa, the ST-1 stress–strain curves develop an inflection point,

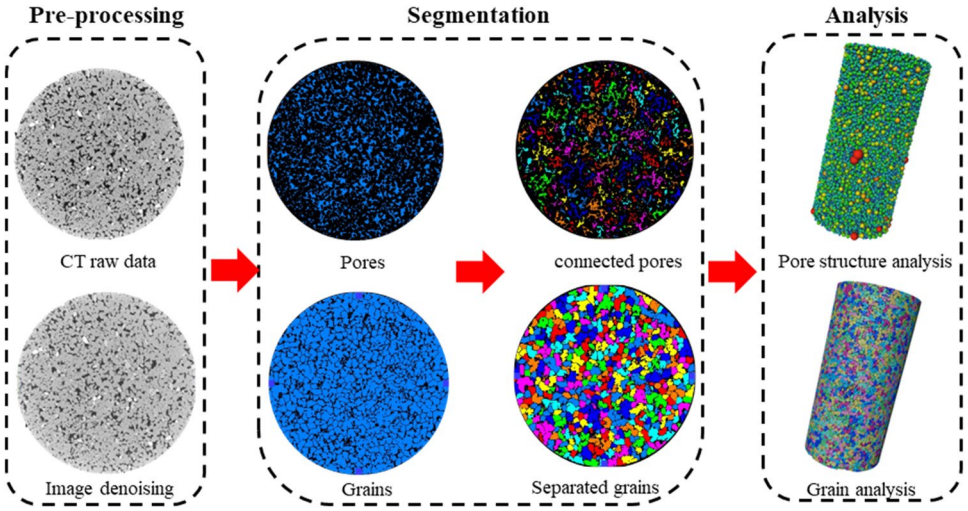

Fig. 5 Schematic diagram of the overall process of sandstone CT processing

demonstrating pronounced, downward concave behaviour. This shift indicates that the stress exceeds the yield point of St Bees Sandstone, marking a transition from elastic to elasto-plastic deformation. Upon reaching differential stress of 42 MPa, a slight downward concave stress–strain behaviour is observed in CG-1. During stress cycling process, the stress–strain curves of the two sandstones do not overlay but form hysteresis loops, indicating the energy dissipation and internal structural changes due to accumulation of inelastic strain. Initially, both, CG-1 and ST-1 exhibit a higher strain accumulation rate at the onset of stress cycling, resulting in larger hysteresis loops and a notable increase in inelastic strain accumulation during 1st compared to subsequent cycles. Additionally, inelastic deformation continues to accumulate over successive cycles, albeit at a diminishing rate, eventually reaching a stabilized state. Consequently, the inelastic hysteresis loops progressively narrow, approaching each other, and eventually overlaps as the number of loading cycles increases. The slope of the unloading curve becomes roughly the same as that of the loading curve, which was also reported in previous studies (Liu et al. 2020; Yang et al. 2019). Throughout the cyclic loading process, ST-1 accumulates more total axial strain and inelastic strain compared to CG-1. In addition, the unloading curve at the 5th cycle of ST-1 does not align with the loading curve at the 6th cycle, possibly due to microcracks opening during the unloading process (Zhang et al. 2023).

To further investigate the effects of confining pressure and cyclic amplitude on the properties of the two types of sandstone, we conducted two sets of full-stress cycling tests under different levels of confining pressure (10.5 MPa and 19.5 MPa) and calculated the accumulation of inelastic strain and the evolution of Young's Modulus for each cycle. At a confining pressure of 10.5 MPa, both CG-2 and ST-2 show non-linear upwardly concave stress–strain behaviour during the initial loading, similar to in situ stress conditions. As differential stress reaches a certain level, both samples exhibit downward concave stress–strain behaviour. During the cyclic process, the inelastic strain in both sandstones was largest in the 1 st cycle, decreasing gradually with subsequent cycles. In contrast, no apparent upward concave stress–strain behavior was observed for CG-3 at a confining pressure of 19.5 MPa. This is because the increased confining pressure facilitates the rapid closure of internal microcracks and pores within the sandstones, thereby enhancing their overall stiffness, allowing the stress–strain curve to reach the linear elastic zone more quickly (Peng et al. 2015). After 5 cycles, the inelastic deformations in CG-2 and ST-2 increases to 0.63% and 0.78% (Fig. 7a), respectively, showing a marked increase compared to in situ stress conditions, where the accumulated inelastic strain after 5 cycles reaches 0.43% and 0.69% only (Fig. 6a, 6b). This indicates that the accumulation of inelastic strain is significantly influenced by the amplitude of cyclic stress, likely related to the dynamic closing and opening of internal microcracks and pores (Jia et al. 2018). Furthermore, with an increase in stress cycles, both sandstones show a similar trend in Young's Modulus as with inelastic strain, gradually increasing with stress cycles, albeit at a slower rate. After 5 cycles, the Young's Moduli for CG-2 and ST-2 reach 7.12 and 6.52 GPa respectively (Fig. 7b). In contrast, CG-3 and ST-3, which were subjected to a confining pressure of 19.5 MPa, display lower axial total strain and inelastic strain compared to those in the 10.5 MPa group. After 5 cycles, the accumulated inelastic strain was only 0.34% and 0.48%, and their Young's moduli were higher, reaching 8.39 GPa and 7.21 GPa (Fig. 7b), respectively. This discrepancy can be attributed to the higher confining pressure conditions, which bolster the overall strength of the sandstones, resulting in increased yield stress (Huang et al. 2021;

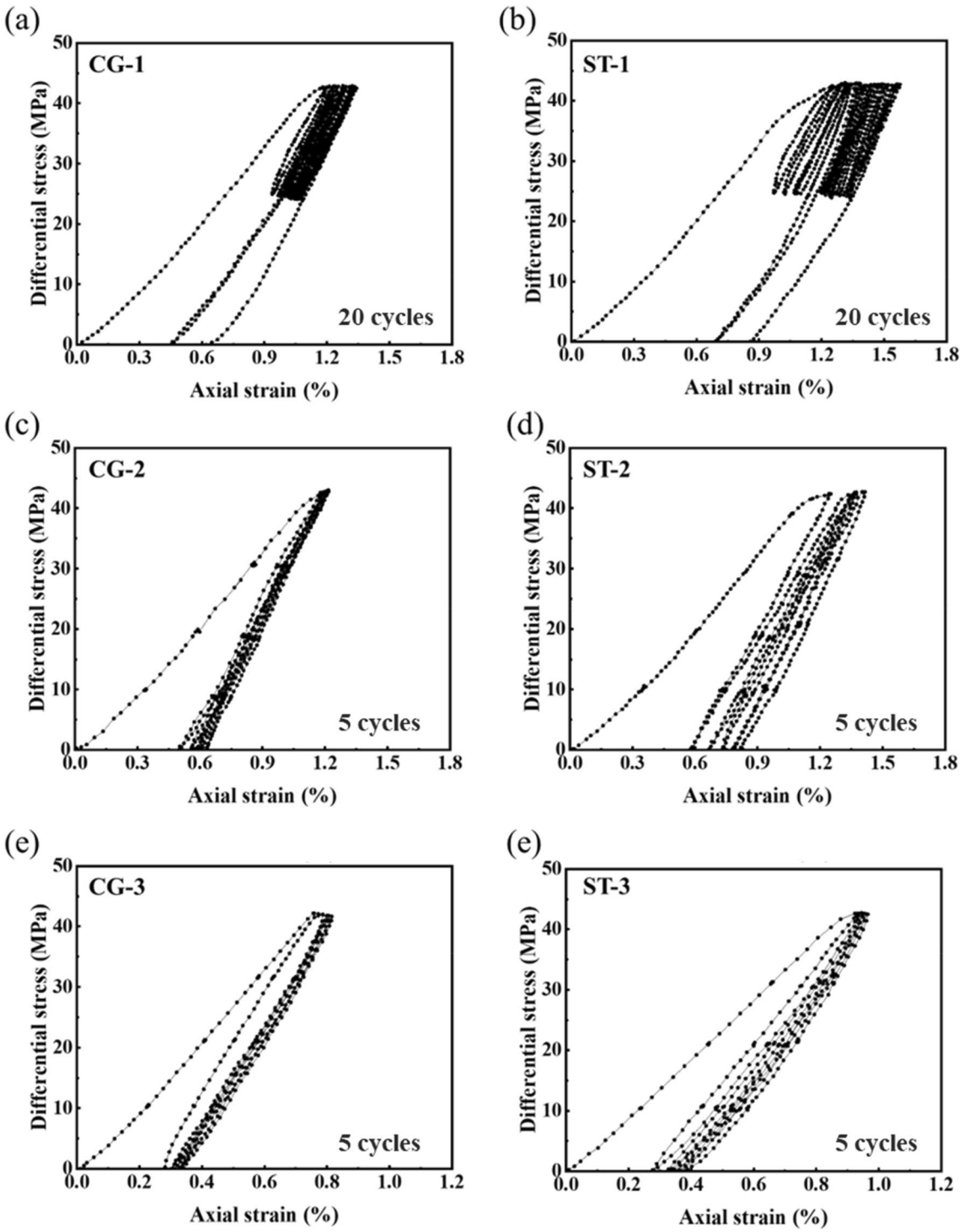

Fig. 6 Stress–strain curves of Castlegate and St Bees Sandstone under various stress conditions. **a**, **b** CG-1, ST-1 under in situ stress conditions. **c**, **d** CG-2, ST-2 fully stress cycling experiments under 10.5 MPa confining pressure. **e**, **f** CG-3, ST-3 fully stress cycling experiments under 19.5 MPa confining pressure

Shirani Faradonbeh et al. 2022). This is evident from the absence of clear inflection points or subsequent concave stress–strain behavior in their stress–strain curves in CG-3 and ST-3. Therefore, both sandstones exhibit smaller inelastic axial strains under the same differential stress conditions. It is noteworthy that under the same confining pressure conditions, St Bees Sandstone

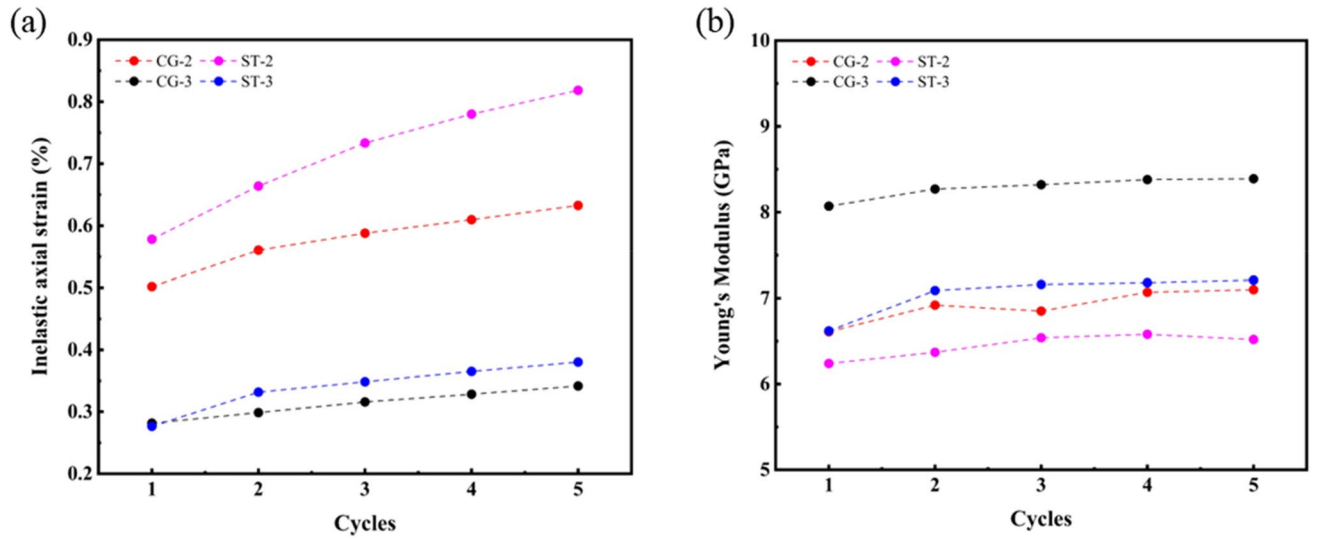

Fig. 7 Evolution of inelastic axial strain as well as Young's Modulus with the number of cycles for Castlegate and St Bees Sandstones. **a** inelastic axial strain with cycles; **b** Young's Modulus with cycles. Young's Modulus is derived from the stress–strain curve in the elastic zone during the unloading process

generally exhibits higher cumulative inelastic strains compared to the Castlegate Sandstone.

3.2 Permeability Evolution

Figure 8 demonstrates the permeability variations of CG-1 and ST-1 over 20 cycles under in situ stress conditions. The black dots in both figures denote permeability measurements taken at low-stress levels (injection phases, Q =25 MPa), while red dots correspond to measurements at high-stress levels (depletion phases, Q=42 MPa). The data indicate a marked reduction in permeability for both sandstones in the first 5 cycles, i.e. the permeability of CG-1 decreases from an initial value of 3.26×10^{-13} to 2.36×10^{-13} m^2 (27.6%) by the 5th cycle at low-stress levels and from 2.64×10^{-13} to 2.12×10^{-13} m^2 (18.9%) at high-stress levels. In comparison, the permeability of ST-1 decreases from 2.0×10^{-13} to 7.83×10^{-14} m^2 at low-stress levels and from 1.28×10^{-13} to 5.61×10^{-14} m^2 at high-stress levels, corresponding to a decrease of 60.8% and 56.8% for CG-1 and ST-1, respectively. After completing 5 cycles, both sandstones were fully unloaded and

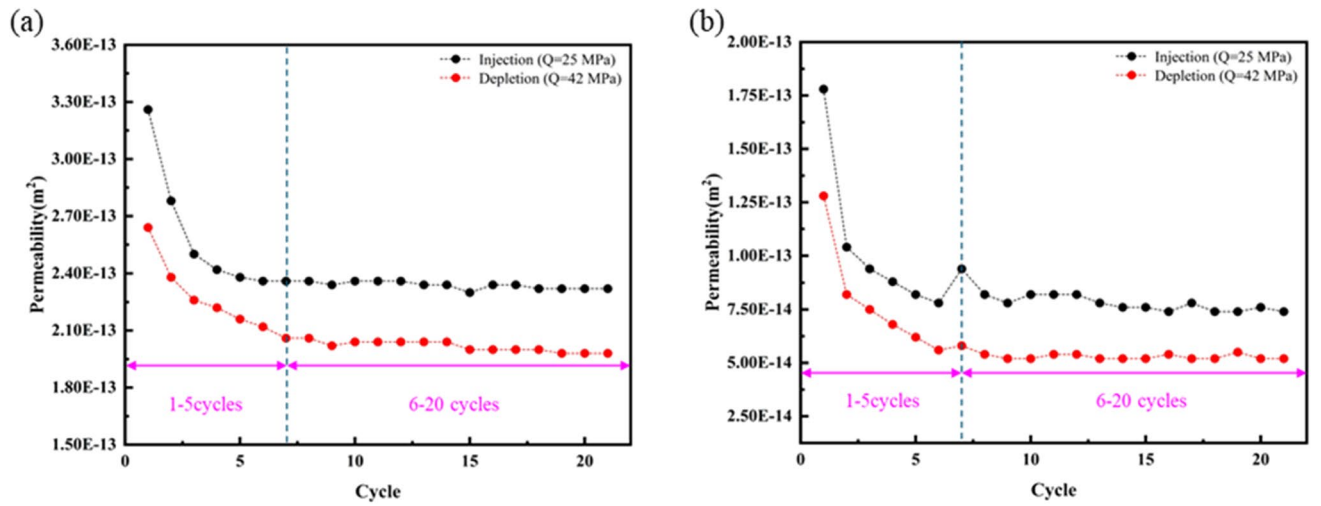

Fig. 8 Permeability variations in Castlegate and St Bees Sandstone samples during loading cycles. **a** Castlegate Sandstone (CG-1), **b** St Bees Sandstone (ST-1). Note that after the 5th cycles, the pressure on the sample was unloaded, and the sample was taken out of the cell for CT scanning

subjected to microscopic structural analysis. Subsequently, the cyclic experiment was resumed. As shown in Fig. 8, as the number of cycles increases, the permeability of both sandstones eventually stabilized. Specifically, the permeability of CG-1 stabilizes at 2.32×10^{-13} m^2 and 1.80×10^{-13} m^2 under low and high stress, respectively. Conversely, ST-1 maintains permeability levels of 7.48×10^{-14} and 5.25×10^{-14} m^2 under low and high-stress conditions, respectively. This phenomenon is attributed to the initial adjustment of microstructures during cyclic loading until reaching a new equilibrium state. In this state, pore and fracture structures become relatively stable, leading to a gradual reduction in permeability changes (Wang et al. 2017). Notably, there was a significant increase in the permeability of ST-1 during the 6th cycle, particularly under low-stress conditions. This increase may be due to the reopening of some microcracks following full unloading in the 5th cycle, thereby enhancing permeable flow pathways (Liu et al. 2020; Popp et al. 2001; Zhao et al. 2019).

Figure 9 illustrates the permeability variations of Castlegate and St. Bees sandstones in response to changing differential stress. The data indicates that during the loading phase, the permeability of both sandstones tends to decrease as the differential stress progressively increases. Notably, the reduction in permeability was most substantial following the initial loading, indicating a heightened sensitivity of the sandstone internal structure to the initial stress response. Although permeability continues to decline with subsequent loading cycles, the rate of this decline diminishes, suggesting that the internal structure of both sandstones does not change significantly following repeated cycles for the conditions tested to repeated stress applications. During the unloading phase, the permeability of both sandstones exhibits gradual recovery as differential stress decreases. However, this recovery does not fully revert to the

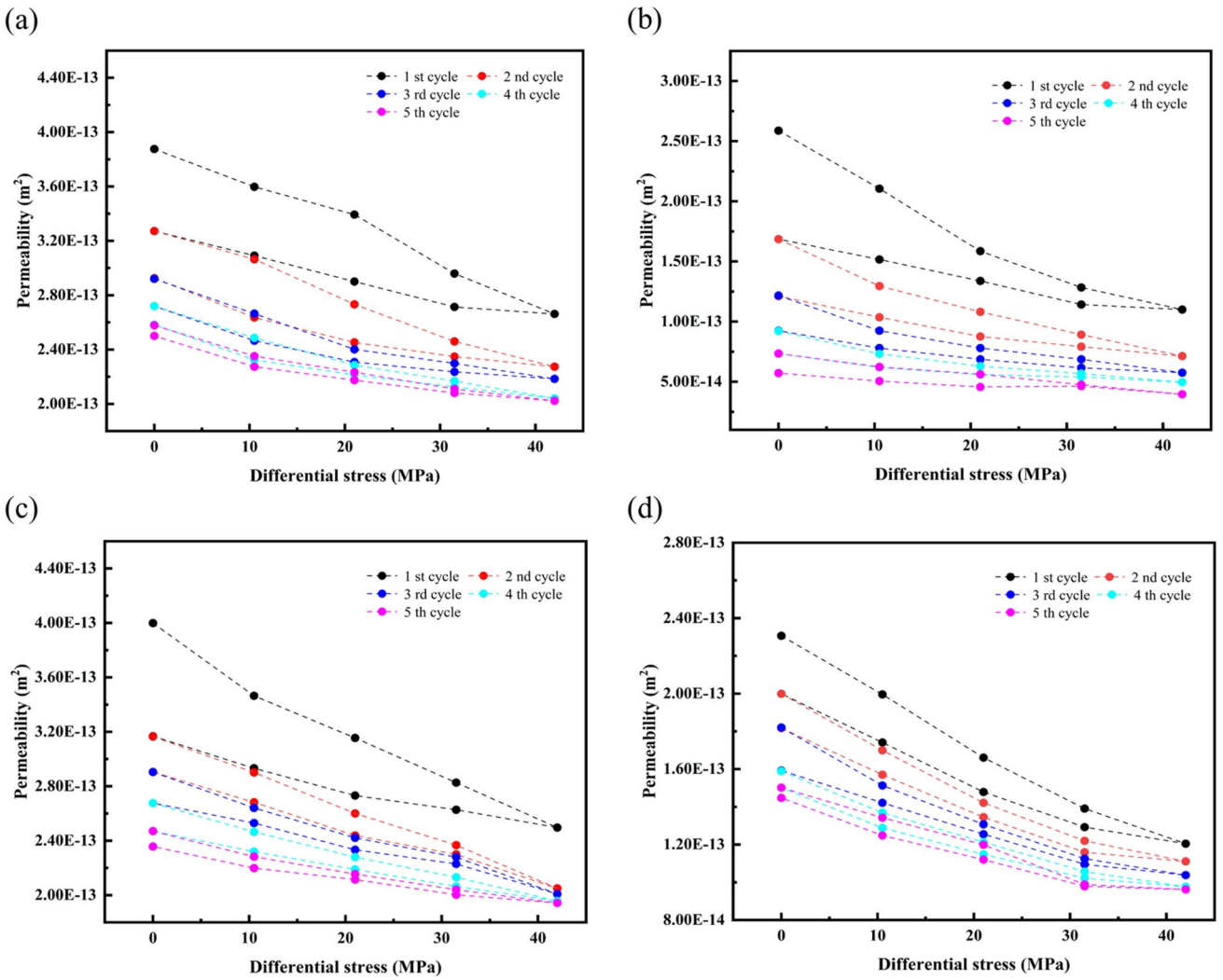

Fig. 9 Permeability evolution following differential stress cycling. **a** Castlegate Sandstone (CG-2), Pc = 10.5 MPa; **b** St Bees Sandstone (ST-2), Pc = 10.5 MPa; **c** Castlegate Sandstone (CG-3), Pc = 19.5 MPa; **d** St Bees Sandstone (ST-3), Pc = 19.5 MPa

original state, manifesting as a pronounced hysteresis loop, with the largest scale of the loop observed in the first loading–unloading cycle. This hysteresis effect could be attributed to compression of the pores plus microcracks within the sandstone during loading, which is not completely reversible in the subsequent unloading process (Dong et al. 2010; Teklu et al. 2016; Wang et al. 2017). With an increase in the number of cycles, the microstructure of both types of sandstones is subjected to an initial period of adjustment, during which the pore structures become relatively stable, leading to a gradual permeability loss. This trend is evidenced by the decreasing magnitude of hysteresis loops. Specifically, for CG-2, experimental data indicate that under a confining pressure of 10.5 MPa, its permeability ranges from 2.05×10^{-13} m^2 (during the 5th cycle, with a differential stress of 42 MPa) to 3.88×10^{-13} m^2 (during the 1st cycle, with a differential stress of 0 MPa), resulting in a 35.5% permanent loss of permeability by the end of the cycles. Under a confining pressure of 19.5 MPa, the initial permeability (during the 1st cycle, with a differential stress of 0 MPa) was 3.99×10^{-13} m^2, which decreases to a minimum of 1.95×10^{-13} m^2 (during the 5th cycle, with a differential stress of 42 MPa), resulting in a permanent permeability loss of 40.9% at the end of the cycles. This trend mirrors the observations from the 10.5 MPa experimental group but with generally lower permeability values.

The permeability of ST-2 ranges from 3.96×10^{-14} m^2 (during the 5th cycle, with a differential stress of 42 MPa) to 2.59×10^{-13} m^2 (during the 1st cycle, with a differential stress of 0 MPa) under a confining pressure of 10.5 MPa. After 5 cycles, its permanent permeability has decreased to 77.9%. In contrast, in the experimental group subjected to a confining pressure of 19.5 MPa, the permeability of ST-3 varies from 9.61×10^{-14} m^2 (during the 5th cycle, with a differential stress of 42 MPa) to 2.31×10^{-13} m^2 (during the 1st cycle, with a differential stress of 0 MPa). After 5 cycles, its permanent permeability loss is 41.5%. Notably, the permeability reduction during the loading and the permanent permeability loss is lower in the group with a 19.5 MPa confining pressure than those observed in the group under 10.5 MPa. This observation contradicts previous findings that the higher the confining pressure, the lower the permeability, and the greater the permeability loss (Alam et al. 2014; Ramezanian and Emadi 2020; Wang et al. 2017). This aspect will be further analysed in the next section in conjunction with the microstructural observations.

4 Discussion

4.1 Microstructural Observations and Porosity Evolution

Experimental data indicate significant differences in the mechanical response and transport characteristics between Castlegate and St Bees Sandstone subjected to identical stress paths. These variances are closely linked to distinct microstructural attributes, including grain size, grain shape, grain arrangement (Masch and Denny 1966; Payton et al. 2022), as well as pore structure features such as pore size, pore shape, and connectivity (Bernabé et al. 2016; David et al. 1993; Shalev et al. 2014). Consequently, we employed micro-scale CT quantitative analysis to investigate the alterations in these microstructural features and delve into the underlying mechanisms.

4.1.1 The Effects of Stress Cycling on the Microstructure

CT cross-sections of Castlegate (CG-1) and St Bees (ST-1) sandstones are shown in Fig. 10. This series of CT images illustrates the micro-structural changes during cyclic loading experiments under in situ stress conditions. From Fig. 10a to Fig. 10f, it can be seen that the microstructure changes for CG-1 before and after cyclic loading. Figure 10a, d reveals the micro-structure prior to loading, showing an even grain distribution. After five loading cycles, a noticeable reduction in the grain spacing and increased grain contact are evident (Fig. 10b, e). Having completed 20 loading cycles, Fig. 10c, f shows that the grain spacing in CG-1 decreases even more, resulting in a densely packed grain arrangement. Notably, there are no visible fractures among the grains, indicating that the integrity of the grains is well preserved. These observations imply that inelastic strain was primarily accommodated through grain rearrangement and sliding in this sandstone to adjust to stress cycling. Conversely, Fig. 10g–f illustrate the microstructural alterations observed in St Bees Sandstone under identical experimental conditions. St Bees Sandstone has a smaller average grain size than the Castlegate Sandstone, alongside poor grain roundness prior to loading tests (Fig. 10g, j). After 5 loading cycles, evident from Fig. 10h, k. the emergence of shear bands—resulting from grain fractures—is marked by areas highlighted with red arrows, illustrating the alignment of fragmented grains along a specific orientation. A further increase in loading cycles to 20 accentuated the shearing effect within St Bees Sandstone, as demonstrated in Fig. 10i and l. This amplification in shearing indicates a proliferation of intragranular and intergranular fractures, with the sandstone's inelastic strain predominantly facilitated by broken grains and, as a result, development of shear bands.

To further investigate the behaviour of the two sandstones at the microscale after in situ conditions, we compared CT images of their vertical sections and three-dimensional porosity variations at different stages, as illustrated in Fig. 11 (Baud et al. 2017; Hu et al. 2022). All images of the vertical

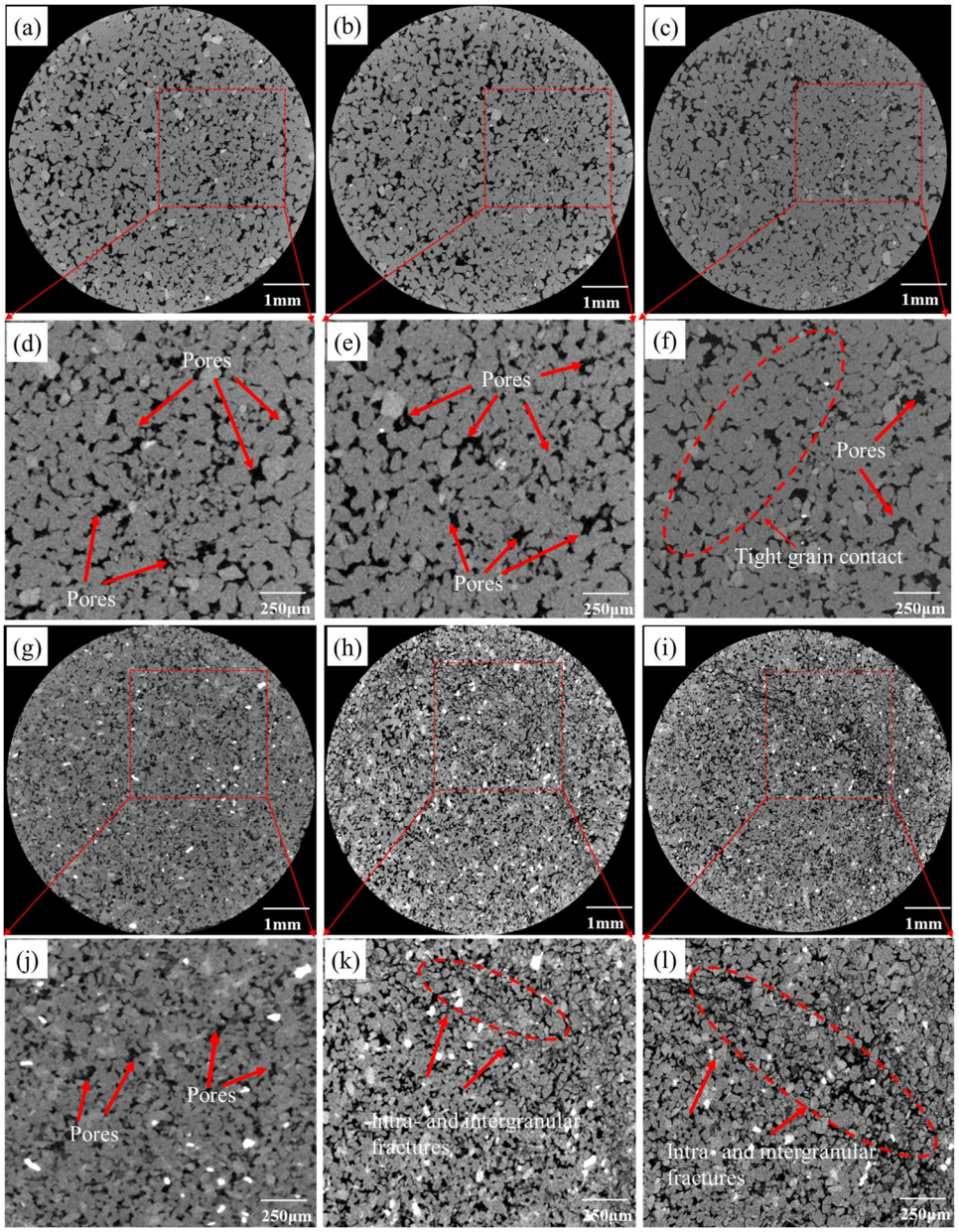

Fig. 10 CT cross-sections for CG-1 and ST-1. **a**, **g** CG-1, ST-1 before the test. **b**, **h** CG-1, ST-1 after 5th cycles. **c**, (i) CG-1, ST-1 after 20th cycles. **d–f**, **j–l** Magnified local areas of the CT images. The local areas are marked by red boxes

sections were taken from the XZ direction of the two sandstones. The spatial distribution of rock porosity was obtained by calculating the planar porosity for each slice and cumulatively stacking these calculations (as illustrated by the red curve). For Castlegate Sandstone, the curve's shape reveals significant porosity fluctuations along its entire length prior to initiating the experiment, with relatively higher porosity at 0–7.5 mm and 15–20 mm sections. Overall, the average porosity is 18.8%, indicating that the porosity distribution of Castlegate Sandstone in its natural state was heterogenous, possibly affected by geological processes or differences in rock composition (Fig. 11a, red curve). After five stress cycles, it can be observed that certain sections of the Castlegate Sandstone are compacted. This results in a porosity curve slightly flatter than before the loading, decreasing the overall porosity slightly to an average value of 18.5% (Fig. 11a, blue curve). After 20 cycles, the porosity of the Castlegate Sandstone declined further, exhibiting significant differential compaction, with a noticeable decline in porosity of 7.5–15 mm compared to other sections, from 18.2% to 17.6%, as shown in Fig. 11a. Consequently, the average porosity reduces to 18.3% (Fig. 11a, black curve). Further CT imaging confirms that the sandstone experienced additional compaction, with an even tighter grain arrangement (Fig. 11b–d).

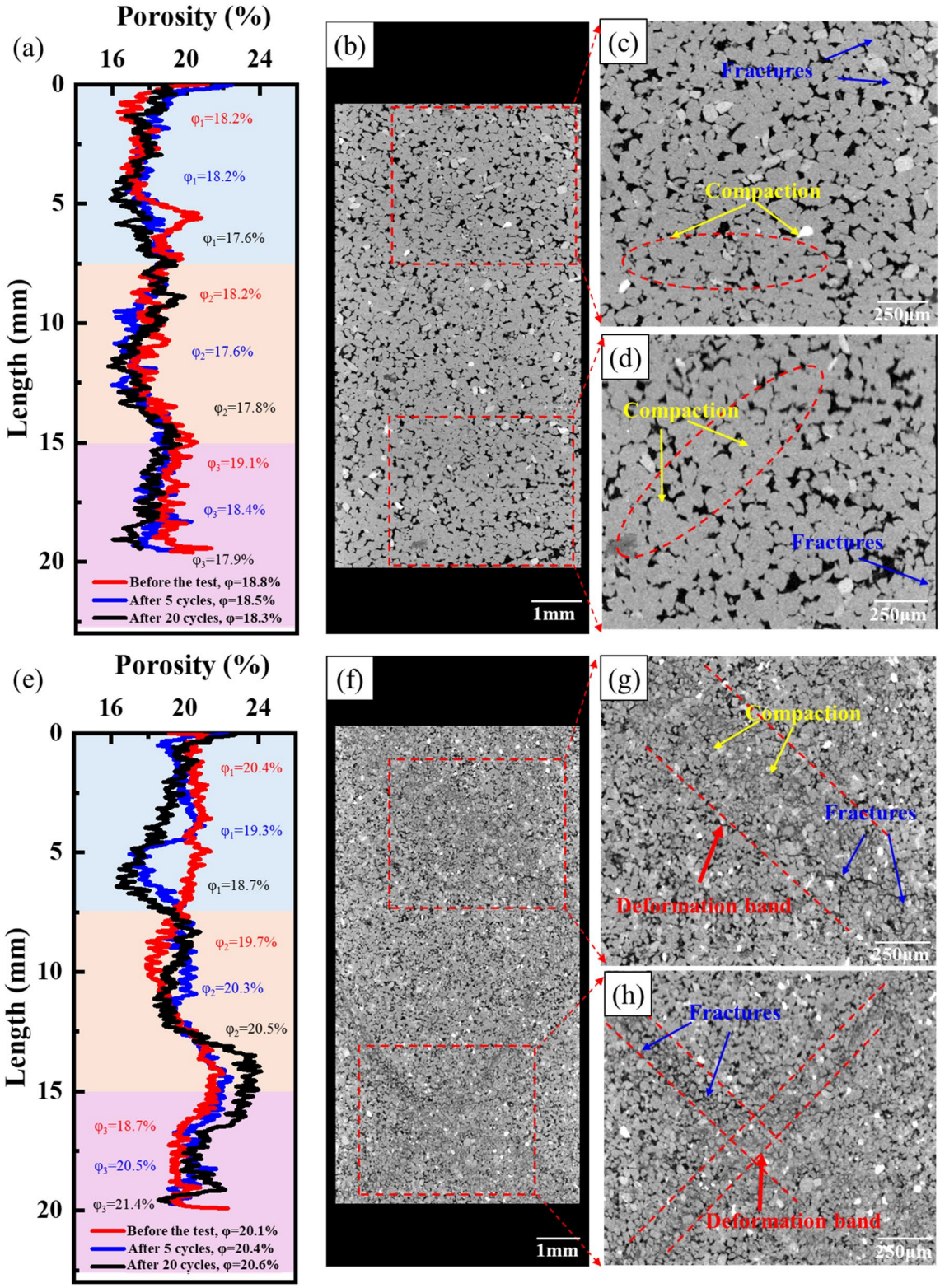

Fig. 11 Porosity variations and vertical CT images after in situ stress conditions. **a** Porosity evolution of CG-1 during the experiments. **b–d** Vertical CT images of CG-1 after 20 cycles. (**e**) Porosity evolution of ST-1 during the experiments. **f–h** Vertical CT images of ST-1 after 20 cycles. φ_1, φ_2, and φ_3 represent the local porosity in the 0–7.5 mm, 7.5–15 mm, and 15 mm to the bottom of the sandstone segment, respectively. The colour indicates the loading state, with red φ representing 0 cycles, blue φ after 5 cycles, and black one after 20 cycles

In comparison, the porosity of St Bees Sandstone also exhibits spatial heterogeneity prior to the experiments, especially from 5 to 10 mm where lower porosities are clearly evident in Fig. 11e. Nevertheless, the overall average porosity of St Bees Sandstone remains higher than that of the Castlegate Sandstone, reaching 20.1% (Fig. 11e, red curve). After five stress cycles, significant changes are observed in the spatial distribution of porosity: a decrease within the 4–8 mm sections and an increase within the 10–15 mm sections. Consequently, the average porosity experiences a slight increase, reaching 20.4%, compared to the pre-experimental phase (Fig. 11e, blue curve). As the experiments proceed to 20 cycles, the alterations in St Bees sandstone's porosity becomes more pronounced. The porosity in the 0–7.5 mm section decreases from 19.3% to 18.7%, while the porosity in the 15–20 mm section significantly increases from 20.5% to 21.4%. The overall average porosity rises to 20.6%, with the sandstone exhibiting clear compartmentalization (Fig. 11e, black curve). The CT images demonstrate that the formation of shear bands in St Bees Sandstone, consisting of fractured grains (indicated by a red arrows), which corresponded to fluctuations in the porosity distribution curve. These broken grains contribute to an overall increase in sandstone porosity. Contrary to Castlegate Sandstone, the micro-mechanism of inelastic strain in St Bees Sandstone was primarily dominated by shear dilatancy, rather than by compaction (Fig. 11f–h).

4.1.2 Effect of Confining Pressure

To investigate the micro-scale mechanisms responsible for inelastic strain accumulation and the differences in permeability of the two sandstones under varying confining pressures, we conducted full stress cycle experiments on these sandstones and analysed the differences in their microstructures under different confining pressures using CT scanning after the experiments. The CT images of the two sandstones are shown in Fig. 12. After 5 cycles, deformation bands were observed within the St Bees Sandstone at a confining pressure of 10.5 MPa, characterised by cracked grains induced through shear compression (Fig. 12e, f, marked by red arrows). These findings indicate that the inelastic deformation observed for St Bees Sandstone is intricately associated with intra- and inter-granular fracturing. Within these deformation bands, we find that the broken grains clog original pore space, which is likely the reason for the significant reduction in permeability (Fredrich et al. 1995; Ngwenya et al. 2003; Vajdova et al. 2004). However, no obvious shear bands were observed within the St Bees Sandstone under a confining pressure of 19.5 MPa. This is because of higher confining pressure increasing the overall strength and stability of the rock, thereby making it more difficult to form shear bands (Paterson and Wong 2005; Wong and Baud 2012). Therefore, the dominant mechanism of inelastic strain in sandstone varies under different confining pressure conditions. In contrast, significant microstructural or pore space differences are not exhibited by the Castlegate Sandstone at either 10.5 MPa or 19.5 MPa confining pressure.

Similarly, we compared the spatial distributions of porosity of Castlegate and St Bees sandstones under two confining pressures (10.5 MPa and 19.5 MPa), following five stress cycles. By comparing the CT images (Fig. 12), we can intuitively observe the relationship between changes in porosity and the micro-structural alterations within the sandstone. Notably, the reduction in porosity of the Castlegate Sandstone under a confining pressure of 19.5 MPa, from 18.5% to 18.2%, was pronounced compared to the decrease at 10.5 MPa, from 18.4% to 17.9% (Fig. 13a). Correspondingly, the permeability loss in Castlegate Sandstone is more significant under a confining pressure of 19.5 MPa (Fig. 9a, c). The CT images demonstrate that higher confining pressures result in closer packing between sandstone grains, reducing pore spacing induced by the increased compaction effect, which, in turn leads to a lower in sandstone permeability (Lander and Walderhaug 1999; Luhmann et al. 2013). On the other hand, the s porosity of the St Bees Sandstone slightly increased under a confining pressure of 10.5 MPa, from 20.1 to 20.4%, although porosity showed a significant decrease in the 5–10 mm sections. In contrast, its porosity remains rather unchanged at 20.1% under the 19.5 MPa confining pressure. It is worth noting that although the St Bees porosity slightly increases from 20.1% to 20.4% at 10.5 MPa confining pressure, its permeability loss is significant, reaching 77.9%. In contrast, permeability loss was only 41.5% under 19.5 MPa confining pressure (Fig. 9b and d). Through the CT images (Fig. 12e–h, Fig. 13c), it can be observed that St Bees microstructure severely suffered from alteration at 10.5 MPa confining pressure after repeated loading, especially in the sections corresponding to the 5–10 mm, where porosity drastically decreases, and the development of shear bands are observed. This indicates that the structural strength of St Bees Sandstone is insufficient to resist the effects of cyclic loading under this confining pressure, leading to irreversible damage to the pore structure, thereby significantly reducing permeability on a macroscopic level (El Bied et al. 2002; Ngwenya et al. 2003; Vajdova et al. 2004). Conversely, the smaller loss of permeability in the St Bees Sandstone at 19.5 MPa confining pressure may result from of compaction and subsequent porosity reduction. Although this is likely, pore channel structures might have retained integrity, and there were no significant deformation bands as observed under a confining pressure of 10.5 MPa, resulting in a relatively smaller permeability loss.

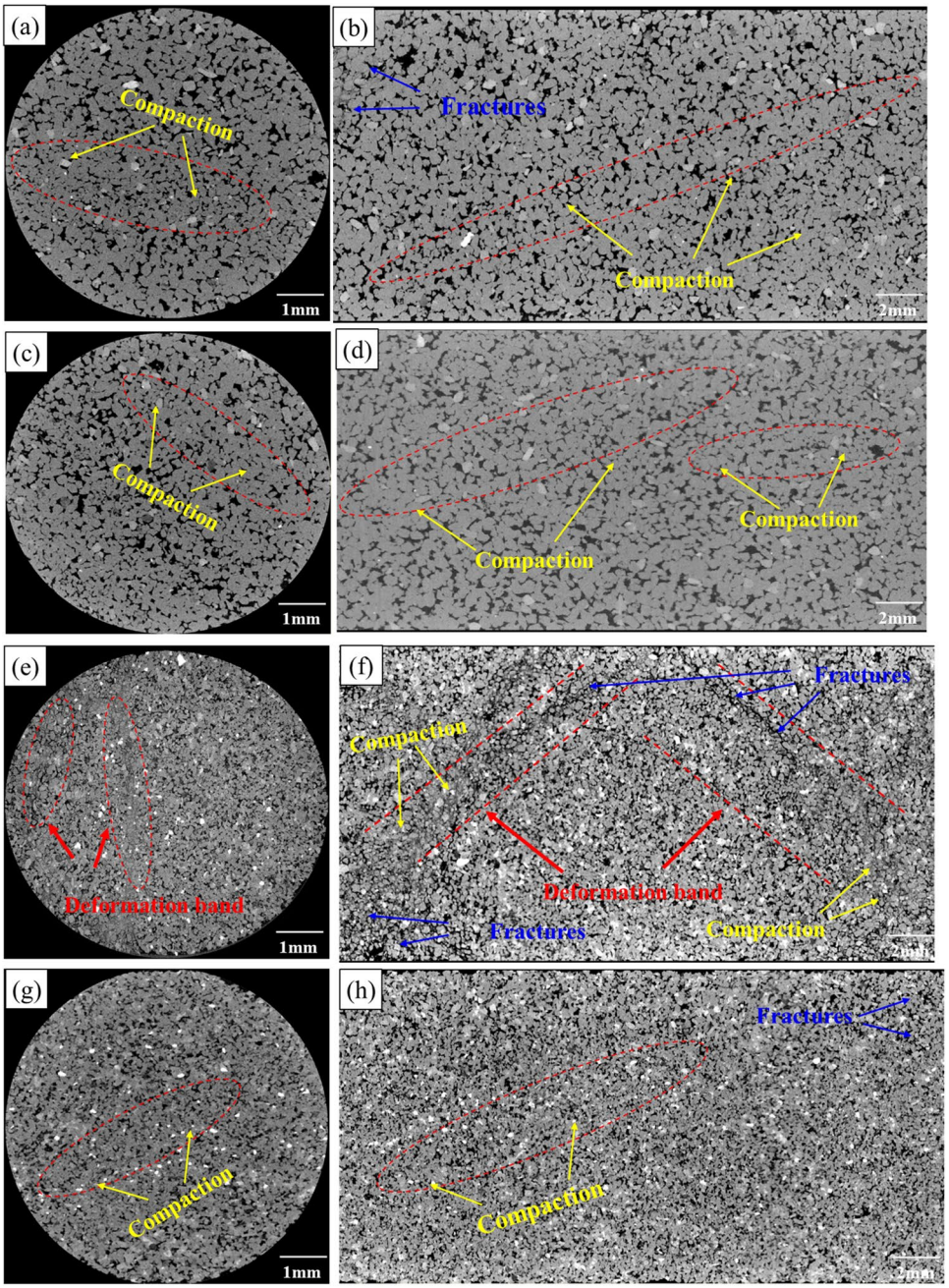

Fig. 12 CT images for Castlegate and St Bees sandstones after fully cyclic loading conditions **a**, **b** CG-2, $P_c = 10.5$ MPa; **c**, **d** CG-3, $P_c = 19.5$ MPa; **e**, **f** ST-2, $P_c = 10.5$ MPa; **g**, **h** ST-3, $P_c = 19.5$ MPa

4.2 Microstructural Variations Under Varying Cyclic Loading Conditions

Microscopic observations, coupled with experimental data, indicate distinct variations in the mechanical responses and transport properties of Castlegate and St Bees sandstones following the same stress paths. Following cyclic loading, both sandstones accumulate varying degrees of axial inelastic strain and experience a reduction in permeability. CT images reveal a close correlation between porosity and permeability changes as well as alterations in the sandstone microstructure induced by inelastic strain. Furthermore, the sandstones display different microstructural changes under varying confining pressure. Previous research indicated that under low-temperature conditions ($T < 150$ °C) and timescales associated with fluid extraction from the upper crust (5 km), inelastic sandstone deformation primarily involves grain-scale processes such as intergranular sliding, rearrangement, and intra- and intergranular cracking (Pijnenburg et al. 2018, 2019; Pijnenburg and Spiers 2020; Wong and Baud 2012, 1999). To quantitatively assess the micro-mechanisms underlying changes in the mechanical and transport

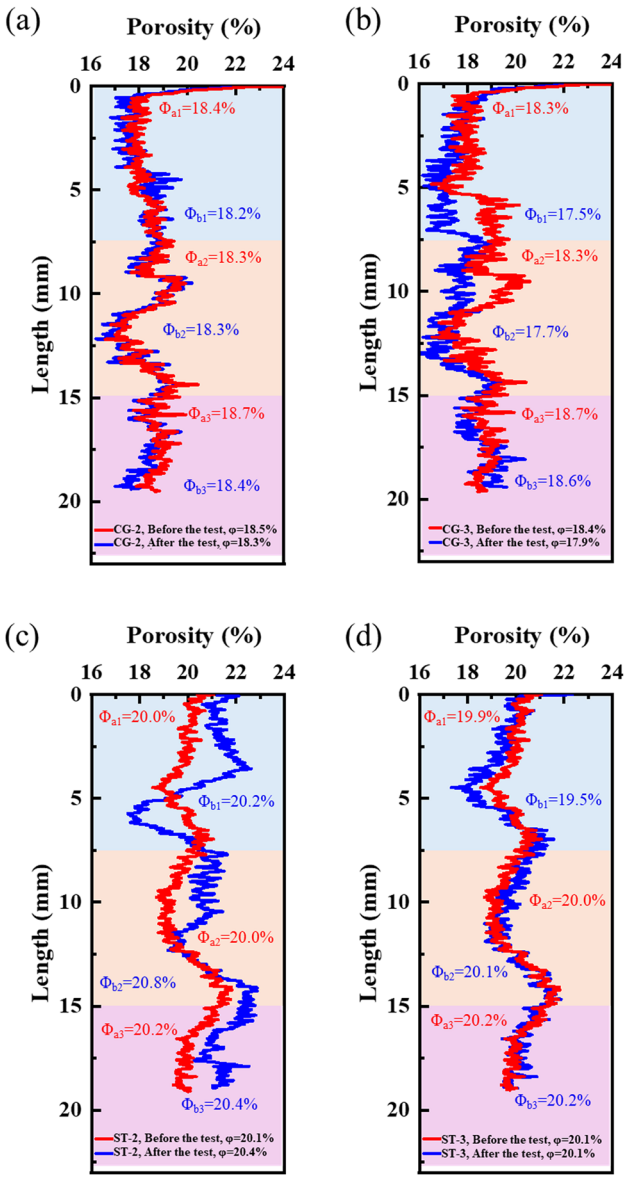

Fig. 13 Porosity variations before and after 5 cycles under fully cyclic loading conditions. **a**, **b** CG-2, $P_c = 10.5$ MPa, CG-3, Pc = 19.5 MPa; **c**, **d** ST-2, Pc = 10.5 MPa, ST-3, Pc = 19.5 MPa. Please note that the ST-2 sandstone was not scanned prior to the experiment; consequently, the porosity curve for ST-2 before the test is, in fact, the porosity curve of ST-3 before loading. As ST-2 and ST-3 are obtained from twin samples at the same depth, it is reasonable to use the porosity curve of ST-3 before the experiment as a proxy for that of ST-2 before the experiment

properties of the two sandstones under cyclic loading conditions, grain analysis was conducted before and after loading under various stress paths. The variations in grain orientation, grain counts, mean grain size, average aspect ratio, and sphericity before and after loading are shown in Table 2.

For clarity, we placed the detailed results of grain analysis in Appendix A. At lower confining pressures (10.5 MPa), no strain localisation was observed after cyclic loading in the coarser grained, highly rounded grains of Castlegate Sandstone (Fig. 12a, b). The grain analysis indicates that the orientation of the sandstone grains changed during the cyclic loading tests (See Appendix A). Additionally, there is no significant variation in grain size and grain number, suggesting that the changes in the microstructure are caused by the movement, rotation, and rearrangement of the sandstone grains in response to these external forces (Table 2). In contrast, discrete shear bands and conjugate shear bands developed in St Bees Sandstone, characterized by higher porosity, smaller grain size (Fig. 12e, f, Fig. 13). Grain analysis shows that the number of grains increased, the average grain size decreased, and the grain sphericity decreased in the St Bees Sandstone before and after the cyclic loading experiments due to widespread grain breakage (Table 2). Additionally, shear band development corresponds to a local porosity decrease, which was also reported previously (Alikarami et al. 2015). Conversely, under higher confining pressures, no significant strain localisation is observed in both sandstones after cyclic loading. Moreover, there were also minor changes in the average grain size and roundness, indicating that the changes in their microstructure were dominated by the movement, rotation, and rearrangement of grains, rather than by dilantancy characterised by widespread grain breakage.

4.3 Evolution of Pore Structure and Effect on Transport Properties

4.3.1 Pore Network Model (PNM)

To investigate the micro-mechanisms responsible for permanent permeability loss, we utilized the Maximum Ball (MB) method for pore network extraction, as developed by Dong and Blunt (2009). This method facilitates a quantitative comparison of pore size distribution before and after exposure to stress cycling. PNMs for CG-1 and ST-1 are illustrated in Fig. 14. Apart from pore size distribution, the topological properties of pores are also crucial for fluid transport in porous media (Bernabé et al. 2016; Yang et al. 2016). The topological structure of pore networks refers to its shape and the way pores are interconnected. Topological properties can be characterized by parameters such as coordination number and tortuosity. Table 3 illustrates these topological parameters before and after loading experiments.

4.3.2 Variations in the Pore/Throat Size

Before experimental testing, Castlegate's pore and throat size distribution were characterized by unimodal patterns. Pore and throat diameters predominantly range between 80–160 and 30–60 µm and are mostly centered around

Table 2 Grain characteristics before and after cyclic loading tests

Sample	Cycles	Number of grains	Mean grain diameter (μm)	Mean sphericity	Mean aspect ratio
CG-1	0	3.18×10^4	266.73	0.77	1.27
	5	3.42×10^4	260.63	0.78	1.29
	20	3.58×10^4	258.76	0.76	1.29
CG-2	0	3.09×10^4	240.86	0.76	1.29
	5	3.24×10^4	226.87	0.78	1.27
CG-3	0	3.17×10^4	271.25	0.77	1.27
	5	3.15×10^4	265.65	0.77	1.27
ST-1	0	3.78×10^4	159.99	0.61	1.31
	5	4.12×10^4	126.52	0.44	2.12
	20	4.35×10^4	106.05	0.32	2.65
ST-2	0	3.63×10^4	167.12	0.59	1.29
	5	4.21×10^4	121.22	0.38	2.60
ST-3	0	3.72×10^4	177.54	0.62	1.31
	5	3.93×10^4	177.12	0.59	1.31

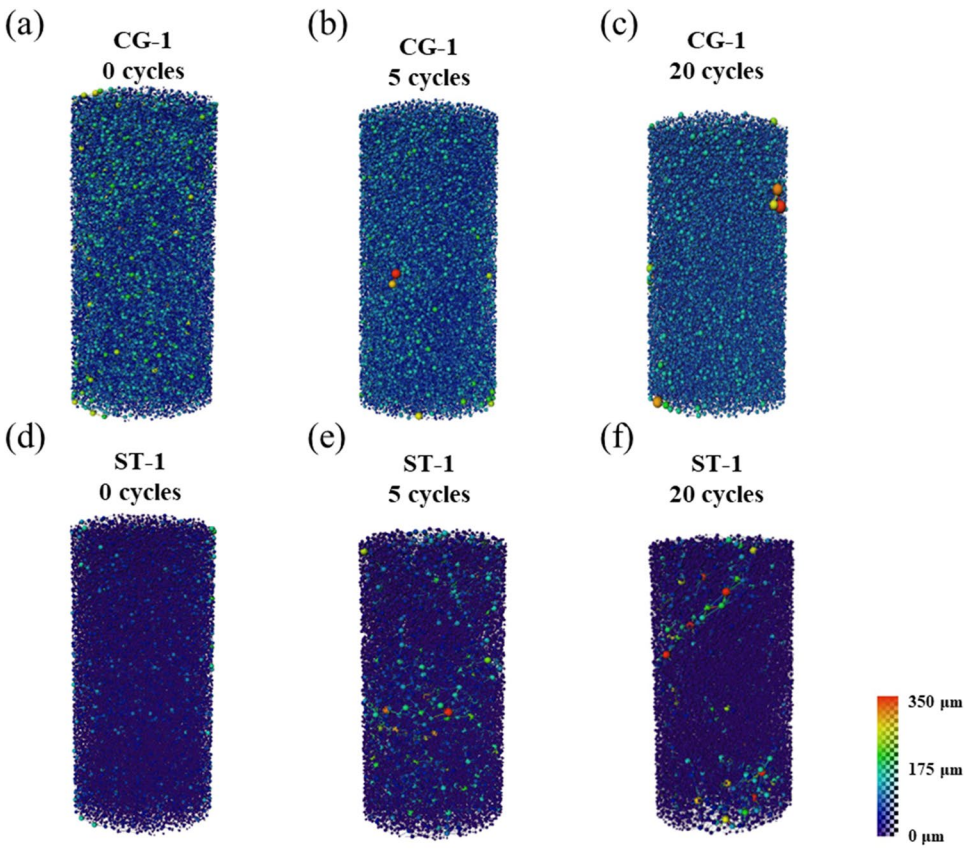

Fig. 14 Pore network model of Castlegate and St Bees sandstones under cyclic loading conditions

120 μm and 40 μm, demonstrating high uniformity and concentration (Fig. 15, Table 3). After five cycles under in situ stress conditions, a noticeable reduction in the number and size of pores and throats of CG-1 was observed, accompanied by a decrease in porosity and a leftward shift in the peak of pore and throat diameter distributions, indicating an overall reduction in their averages (Fig. 15). Such alterations can be attributed to pore and throat compaction due to grain rearrangement under stress cycling conditions (Lander and Walderhaug 1999; Payton et al. 2022; Rice-Birchall et al.

Table 3 Pore structure characteristics of Castlegate and St Bees sandstones under cyclic loading conditions

Sample	Cycles	Number of pores	Total pore volume (μm^3)	Mean pore diameter (μm)	Mean Coordination Number	Number of pore throats	Mean throat diameter (μm)	Tortuosity
CG-1	0	2.79×10^4	2.37×10^{11}	124.78	10.66	1.27×10^5	42.74	1.63
	5	2.66×10^4	2.33×10^{11}	108.23	9.87	1.16×10^5	38.14	1.65
	20	2.62×10^4	2.25×10^{11}	102.17	8.67	1.02×10^5	35.65	1.63
CG-2	0	2.89×10^4	2.44×10^{11}	128.12	10.88	1.39×10^5	42.46	1.63
	5	2.57×10^4	2.31×10^{11}	103.62	9.61	1.08×10^5	37.91	1.65
CG-3	0	2.74×10^4	2.40×10^{11}	131.23	9.78	1.29×10^5	43.21	1.63
	5	2.32×10^4	2.17×10^{11}	105.96	8.46	8.54×10^4	35.18	1.64
ST-1	0	3.75×10^4	2.67×10^{11}	114.67	7.46	1.45×10^5	25.16	1.65
	5	4.22×10^4	2.71×10^{11}	105.78	5.27	1.23×10^5	19.48	1.76
	20	4.35×10^4	2.74×10^{11}	102.45	4.18	1.06×10^5	16.15	1.79
ST-2	0	3.97×104	2.67×10^{11}	107.44	7.87	1.56×10^5	25.72	1.71
	5	4.44×10^4	2.72×10^{11}	100.16	5.24	1.15×10^5	17.18	1.88
ST-3	0	3.82×10^4	2.64×10^{11}	107.25	7.56	1.67×10^5	25.55	1.69
	5	3.63×10^4	2.61×10^{11}	102.17	6.57	1.37×10^5	21.54	1.65

2022). As the loading progresses to 20 cycles, further compaction occurs, albeit less pronounced than in the initial 5 cycles. This suggests an adjustment of the microstructural response to stress cycling. Compared to the in situ stress conditions, CG-2 and CG-3 exhibit similar trends in pore structure variations under fully cyclic loading conditions, with a notable reduction in the number of pores and throats and a decrease in pore/throat size. However, CG-3 demonstrates a more pronounced compaction after 5 cycles. This indicates that higher cyclic stress amplitudes and confining pressures result in more compact pore structures, consequently diminishing fluid flow channels and reducing permeability, narrowing pores and throats, thereby impeding fluid flow channels and diminishing permeability (Dong et al. 2010; Wang et al. 2017). This observation can also be verified by examining sandstone microstructures and the porosity evolution, as illustrated in Fig. 11. The coordination numbers for CG-1, CG-2, and CG-3 decrease under cyclic loading conditions, suggesting that compaction of pores and throats results in diminished connectivity. Additionally, their tortuosity exhibits negligible variation across loading cycles, fluctuating within the range of 1.63 to 1.65, as shown in Table 3. This indicates that the decline in permeability is primarily associated with compaction, leading to an increase in rock strength and narrowing of fluid flow channels. As a result, pore connectivity is reduced and permeability decreases (Lothe et al. 2002; Luhmann et al. 2013; Payton et al. 2022).

Similar to the Castlegate Sandstone, the St Bees Sandstone exhibits a unimodal (but generally smaller) pore/throat size distribution prior to cyclic tests, with the majority of pores and throats ranging between 40–120 and 10–40 μm, respectively (Fig. 16). Under in situ stress conditions and after 5 loading cycles, porosity, and number of pores in ST-1 are significantly increased. Larger pores play a more substantial role in porosity, yet there is a noticeable decrease in throat number and average diameter. This change is attributed to grain cracking induced by shear dilatancy, leading to the formation of larger pores and an overall increase in porosity (Wong and Baud 2012, 1999). Additionally, fine debris generated from grain cracking fill and block throats, thereby contributing to a decrease in both throat number and average diameter (Fowles and Burley 1994). This interpretation is supported by microstructural observations, as illustrated in Figs.10–12. After 20 loading cycles, pore number and porosity continue to increase while throat number decreases. However, the extent of this increase is significantly less compared to the first 5 cycles (Table 3, Fig. 16) and considered to be attributed to the formation of an interlocking structure among the fractured grains, reaching a state of equilibrium (El Bied et al. 2002; Fowles and Burley 1994; Scholtès and Donzé, 2013). Under the same confining pressure, ST-2 exhibits similar trends in pore structure changes, i.e., increased pore number and porosity but decreased throat number. Notably, compared to ST-1 and ST-2, ST-3 displays different changes after 5 cycles under full stress conditions, with reductions in pore number, porosity, and throat number (Fig. 16). Additionally, it exhibits a superior pore topology, characterised by a higher average coordination number and lower tortuosity, accounting for its higher permeability than the former (Table 3). Microstructural observations reveal that no significant shear bands develop within ST-3 sandstone under this stress path, indicating that pore changes are primarily driven by compaction rather than dilatancy (Fig. 12g–h). Therefore, permeability loss is mainly related to pore compression and the closure

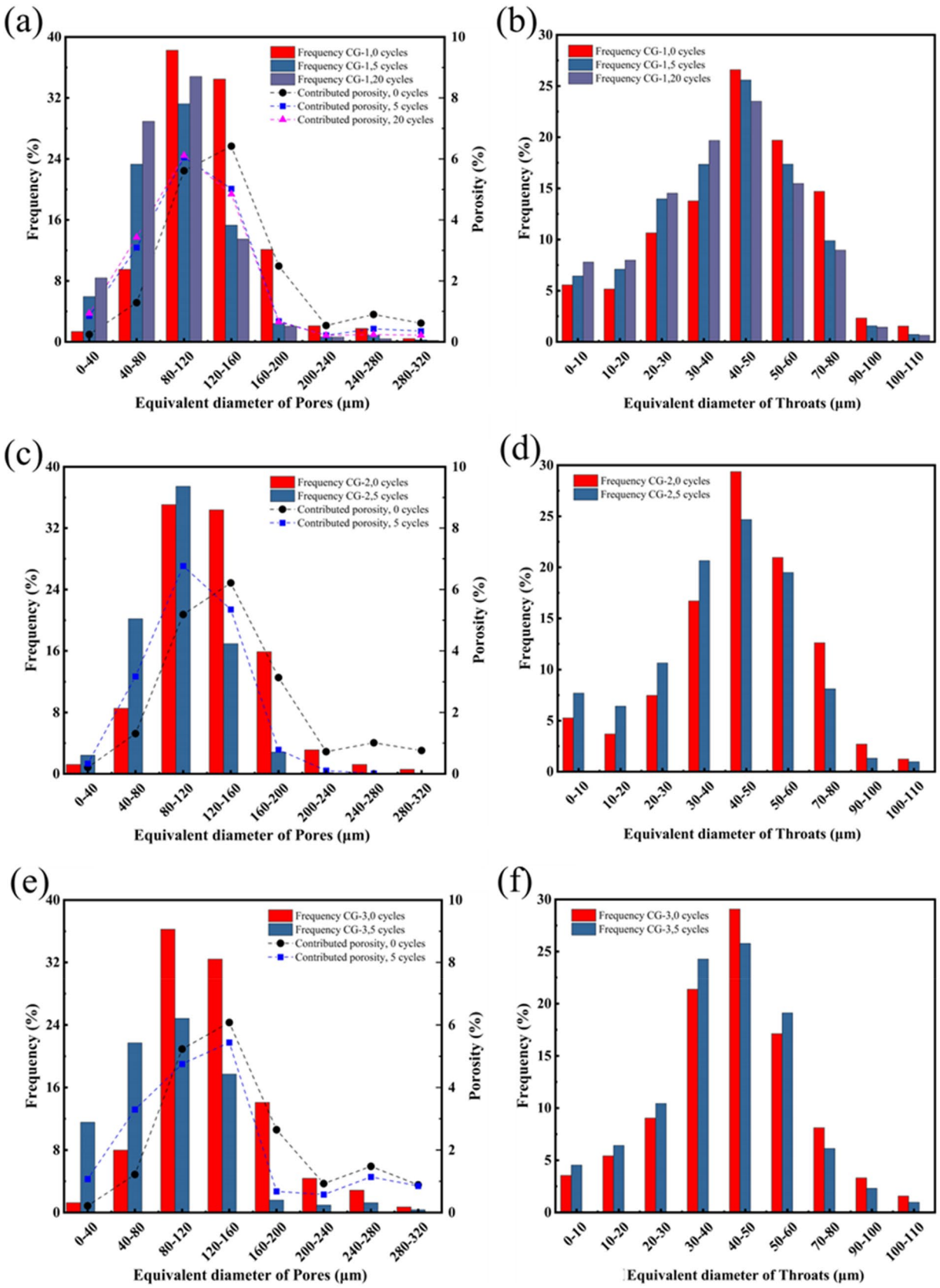
(a)
Frequency CG-1,0 cycles
Frequency CG-1,5 cycles
Frequency CG-1,20 cycles
Contributed porosity, 0 cycles
Contributed porosity, 5 cycles
Contributed porosity, 20 cycles
Frequency (%)
Porosity (%)
0-40
40-80
80-120
120-160
160-200
200-240
240-280
280-320
Equivalent diameter of Pores (μm)
(b)
Frequency CG-1,0 cycles
Frequency CG-1,5 cycles
Frequency CG-1,20 cycles
Frequency (%)
0-10
10-20
20-30
30-40
40-50
50-60
70-80
90-100
100-110
Equivalent diameter of Throats (μm)
(c)
Frequency CG-2,0 cycles
Frequency CG-2,5 cycles
Contributed porosity, 0 cycles
Contributed porosity, 5 cycles
Frequency (%)
Porosity (%)
Equivalent diameter of Pores (μm)
(d)
Frequency CG-2,0 cycles
Frequency CG-2,5 cycles
Frequency (%)
Equivalent diameter of Throats (μm)
(e)
Frequency CG-3,0 cycles
Frequency CG-3,5 cycles
Contributed porosity, 0 cycles
Contributed porosity, 5 cycles
Frequency (%)
Porosity (%)
Equivalent diameter of Pores (μm)
(f)
Frequency CG-3,0 cycles
Frequency CG-3,5 cycles
Frequency (%)
Equivalent diameter of Throats (μm)

◂**Fig. 15** Pore body and pore throat evolution in Castlegate Sandstones before and after cyclic loading. **a**, **c**, **d** respectively represent the pore size distributions and their porosity percentages of CG-1, CG-2, and CG-3; **b**, **d**, **f**, respectively, represent the throat distributions of CG-1, CG-2, and CG-3

of microcracks. However, in ST-1 and ST-2 sandstone, shear bands caused by the grain fracturing and the grain movement are observed. These fragmented grains fill throats, acting as physical barriers that impede fluid flow, significantly reduce connectivity, and deteriorate the rock's internal structure (Vajdova et al. 2004; Zhu and Wong 1996, 1997). It is these changes in the internal structure that lead to complicate the pore structure of ST-1 and ST-2, thereby resulting in permeability loss.

4.3.3 Micro-mechanisms Control on Transport Property Evolution

Although the Castlegate and St Bees sandstones exhibit a similar trend showing lower permeability with increasing stress level and number of cycles, the underlying micro-mechanisms governing these changes are different. Micro-CT images combined with grain analysis indicate that permeability variation of Castlegate is associated with pore and throat compression caused by grain rotation and rearrangement. Furthermore, the porosity evolution is positively correlated with permeability change. Conversely, for St Bees under low confining pressure, permeability variation is closely related to the development of shear bands, and porosity evolution negatively correlates with permeability change. Despite the expansion of pore space, permeability continues to decline. Zhu and Wong (1997) proposed that, unlike compact rocks, high-porosity sandstones exhibit a positive correlation between porosity and permeability during the initial stage under triaxial loading conditions. However, beyond the differential stress reaches C′, at which the curve starts to deviate from a straight line and cracks begin to propagate, marking the onset of dilantancy, permeability continues to decrease even as pore space dilated. To describe the permeability evolution during shear dilatancy in porous rocks, Zhu and Wong (1997) introduced a dimensionless parameter ξ:

$$\xi = \frac{k(peak)}{k(C')} - 1 \tag{7}$$

where $k(peak)$ and $k(C')$ are permeability at peak stress and stress up to C′, respectively. When $\xi > 0$, permeability increases with the development of dilatancy, showing a positive correlation with porosity, and vice versa. In sandstones with porosity > 15%, permeability evolution has been reported to negatively correlate with porosity ($\xi < 0$) (David et al. 1993; Wong and Zhu 1999; Zhu and Wong 1996, 1997). Despite similar porosity between Castlegate and St Bees Sandstone, the latter exhibits lower strength. As the differential stress increases, it reaches the critical stress threshold C′ for shear dilatancy earlier compared to Castlegate Sandstone. Under lower confining pressures, we find that shear bands develop in St Bees Sandstone, formed by intra- and intergranular fracturing clusters. These clusters would progressively increase during the post-peak stage, culminating in the formation of continuous fractures, ultimately resulting in sample failure. However, before sample failure, these localised shear bands, while inducing pore space dilation, concurrently block pore throats with fractured debris, thereby diminishing pore connectivity, increasing tortuosity, and diminishing hydraulic radius. With increasing confining pressure, the strength of St Bees increases, causing an increase in stress level at the onset of shear dilatancy (Gowd and Rummel 1980; Kranz 1980; Shirani Faradonbeh et al. 2022). Consequently, shear bands are not observed in ST-3 after cyclic loading. In contrast, the magnitude of cyclic differential stress failed to reach the stress level C′ for shear dilation in Castlegate Sandstone. Microstructural changes in this sandstone are induced by grain rotation, movement, and rearrangement. As such, compaction-dominated deformation leads to pore and throat compression, thus establishing a positive correlation between porosity and permeability.

4.4 Implications for Subsurface Hydrogen Storage

Associating the stress path with the shear yield/failure criteria and volumetric failure criteria, as well as the transition zone between them, can help predict the deformation and failure behaviour of rocks. This is particularly relevant under different injection and extraction conditions in UHS. Such an association enhances the understanding of rock strength evolution, porosity changes, and permeability variations, which provides theoretical support for the stability assessment of UHS reservoirs and the optimisation of hydrogen injection and extraction processes.

In this study, the Mohr–Coulomb criterion is integrated with the cap model to evaluate rock failure under different stress paths. The Mohr–Coulomb criterion is a well-established framework for characterising the yield and failure behaviour of materials subjected to shear stress (Fjaer et al. 2008; Fossen 2016). It can be expressed as follows:

$$\tau = \sigma \tan \varphi + c \tag{8}$$

where τ is the shear stress, σ is the normal stress, φ is the internal friction angle, and c is the cohesion. For CG Sandstone, the internal friction angle and cohesion are derived from previous experimental studies (Papamichos et al. 2023; Van den Hoek et al. 2000), with $\varphi = 34°$ and $c = 10$ MPa. The internal friction angle for ST Sandstone is estimated from

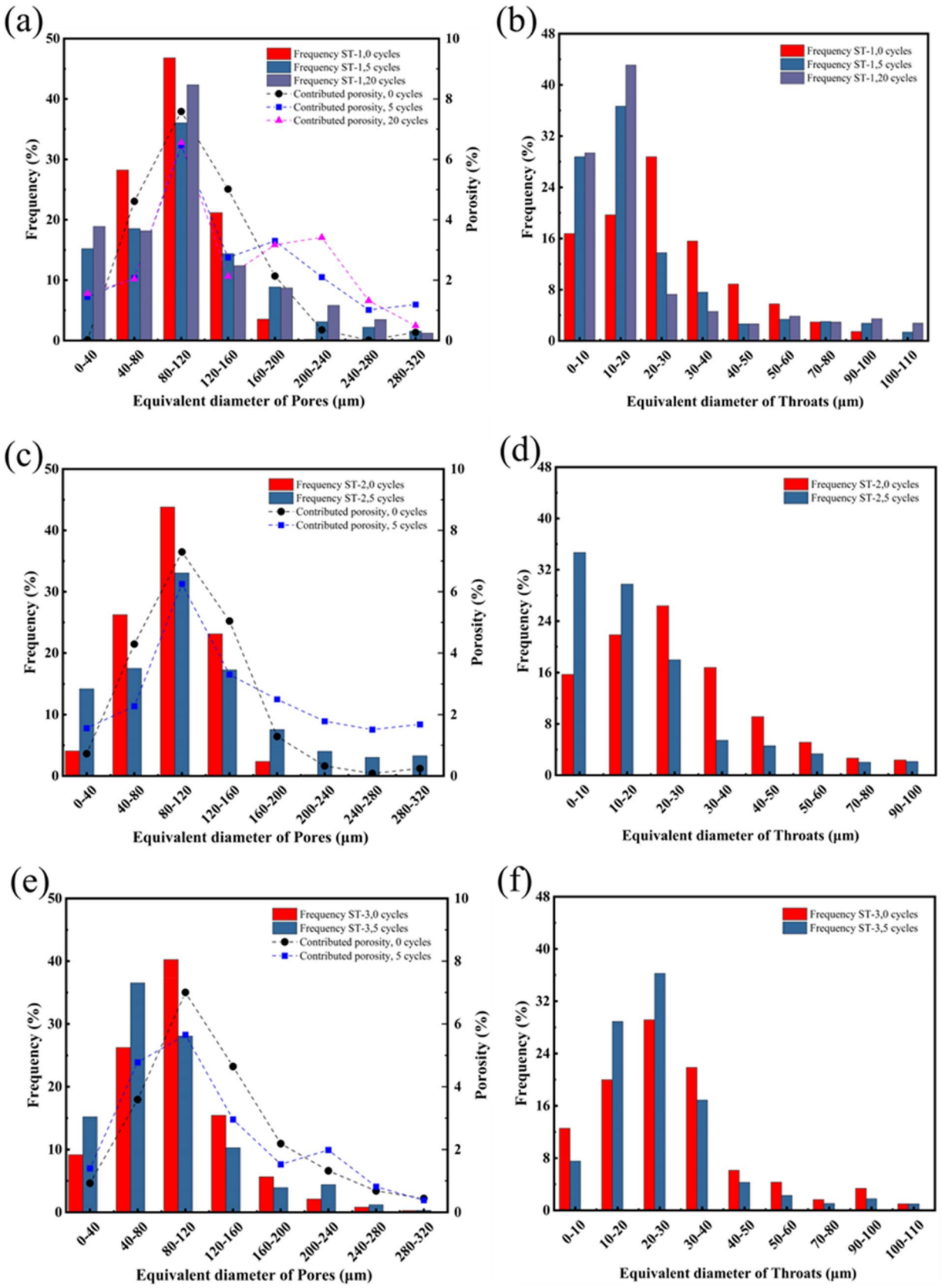

Fig. 16 Pore body and pore throat evolution in St Bees Sandstones before and after cyclic loading. **a**, **c**, **e** respectively represent the pore size distributions and their porosity percentages of ST-1, ST-2, and ST-3; **b**, **d**, **f** respectively represent the throat distributions of ST-1, ST-2, and ST-3

its uniaxial compressive strength (UCS), also based on prior experimental work (Baker 2004; Esterhuizen et al. 2013; Hawkins and McConnell 1991), and is found to be φ = 31.4°, with a cohesion of 14 MPa.

The cap model used in this study is the elliptical pressure cap proposed in previous research (Chen and Mizuno 1990), and its expression is as follows:

$$\frac{(p' - L)^2}{(p_c - L)^2} + \frac{R^2 J_2}{(p_c - L)^2} = 1 \tag{9}$$

where p' represents the mean effective stress, and J_2 denotes the second deviatoric stress invariant. p_c refers to the grain crushing/pore collapse hydrostatic stress, while L indicates the position of the ellipse centre in the hydrostatic stress axis. R is the ratio of the major over minor axes of the ellipse.

The elliptical equation defines the boundary of compaction failure. When the stress path reaches the cap surface, the rock undergoes compaction failure. Due to limited data, the parameters for the cap models of both sandstone types are referenced from previous experimental studies. The cap model parameters for CG Sandstone are obtained from (Papamichos et al. 2023), while those for ST Sandstone are based on similar porosity and grain size sandstone data from (Wong et al. 1997) and (David et al. 1994).

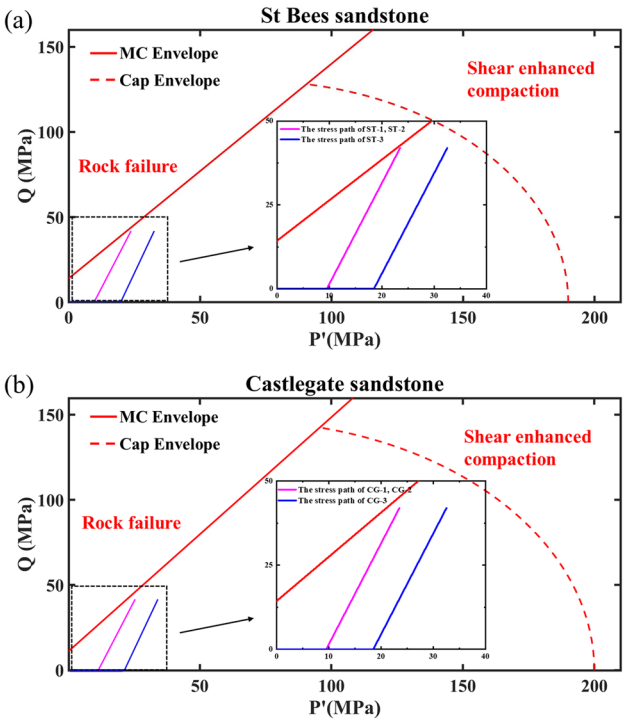

Fig. 17 The failure envelopes and stress paths of the Castlegate and St Bees sandstone in the P′-Q space **a** St Bees Sandstone (ST-2); **b** Castlegate Sandstone

The failure boundary of the rocks is defined through the shear failure envelope (red line) and the compaction cap envelope (red dash line), as illustrated in Fig. 17. Experimental results indicate that, under a constant confining pressure of 10.5 MPa, the stress paths of ST-1 and ST-2 sandstone are close to the shear envelope. Although no macroscopic failure was directly triggered, micro-CT observations reveal the development of numerous shear bands within ST-1 and ST-2 sandstones. These shear bands form as a result of damage accumulation induced by differential stress during cyclic loading, leading to subcritical crack growth and fatigue effects (Figs. 11, 12). These shear bands, composed of broken grains, contribute to throat blockage and a significant decrease in permeability. Therefore, in UHS operations, it is crucial to control the injection-extraction pressure differential to avoid loading near the shear zone, thereby preventing significant permeability loss. Furthermore, with prolonged cyclic loading, the sandstone exhibits "brittle-damage" behaviour, with shear damage accumulation potentially causing a shift in the shear envelope towards lower pressures, thereby reducing the shear strength of the reservoir and leading to failure.

In contrast, CG Sandstone exhibits significantly higher strength, with the stress paths (CG-1, CG-2, CG-3) consistently remaining away from the shear envelope. Experimental results show that the permeability loss in CG Sandstone is primarily due to inelastic strain caused by grain sliding and rearrangement, rather than ductile hardening or brittle fracture. This mechanism is more pronounced under high confining pressures, such as in CG-3, where more intense pore compression and grain contact adjustments are observed. Due to the absence of distinct shear bands development, the mechanical response of CG Sandstone is closer to a “quasi-brittle-grain rearrangement” behaviour. The high-strength characteristics inhibit shear failure, but inelastic strain due to grain rearrangement may lead to adjustments in the cap envelope shape. Further experiments are needed to confirm the direction of this evolution. Despite its high shear resistance, the inelastic deformation driven by grain rearrangement under high confining pressure accelerates pore closure, necessitating control over the injection-extraction rate to mitigate permeability loss.

This study provides a series of insights into the mechanisms related to cyclic pressurization/depressurization of underground hydrogen storage reservoirs. Firstly, both types of sandstone exhibit the most pronounced mechanical response during the first few cycles, gradually stabilizing as loading cycles increase. The gradual increase and eventual stabilization of inelastic axial strain and Young’s Modulus with loading cycles demonstrate the ability of the storage reservoir to adapt to gas injection and withdrawal. However,

it also emphasizes the need for continuous monitoring of reservoir mechanical characteristics, especially during the initial stages of cyclic loading, to ensure reservoir stability. Additionally, the design and operation of underground hydrogen storage reservoirs require thorough consideration of the reservoir petro-properties, stress path history, and potential variations associated with stress cycling. Reservoirs with different rock properties may exhibit diverse changes in mechanical and transport properties under similar stress paths. In this research, the variations in mechanical and transport properties of Castlegate Sandstone are associated with deformation dominated by compaction. Grain movement, rotation and rearrangement induced by stress cycling led to compression of fluid flow paths, resulting in some porosity and permeability reduction. This suggests a potential deceleration of gas diffusion within the reservoir, consequently undermining the efficiency of gas injection and withdrawal processes. To address this challenge, reservoir operation might require strategies aimed at increasing permeability to enhance gas mobility. In contrast, deformation in St Bees Sandstone is predominantly governed by shear dilatancy, characterized by shear band formation that can harm reservoir stability and increase the likelihood of faulting. Additionally, permeability reduction caused by grain fracturing is irreversible, which is unfavorable for underground hydrogen storage operations. Hence, the design and operation of underground hydrogen storage reservoirs necessitate meticulous consideration of reservoir rock conditions. By conducting in-depth analysis and understanding of reservoir rocks, more suitable hydrogen storage areas can be selected, and effective reservoir management strategies formulate to ensure the long-term stability and reliability of hydrogen storage systems.

5 Conclusion

This study provides a comprehensive analysis of the mechanical responses and permeability evolution of Castlegate and St Bees Sandstone under cyclic loading at high stress levels. The key findings are outlined below:

1. Both sandstones exhibit hysteresis loops in the stress–strain curves during cyclic loading, with the hysteresis loop of St Bees being greater than that of Castlegate Sandstone. Additionally, the inelastic axial strain and Young's Modulus of both sandstones increases with the number of loading cycles, with the most significant changes observed within the 1st cycle, followed by a trend towards stability.
2. The permeability of both sandstones decreases with increasing stress and number of loading cycles. For Castlegate, elevated confining pressure leads to an increased permeability loss; whereas for St Bees, permeability loss under high confining pressure is less compared to low confining pressure, which is closely related to the development of shear bands.
3. Microstructural analysis revealed that microstructural alterations for Castlegate are caused by grain movement, rotation, and rearrangement under external forces, resulting in pore/throat compression and a porosity and permeability decrease. Microstructure changes of St Bees Sandstone under low stress conditions are attributed to grain cracking caused by shear dilatancy. Despite an increase in porosity due to shear dilatancy, fractured debris block throats, complicating pore structure and significantly reducing permeability. The strength of St Bees Sandstone increases under high confining pressure and the absence of sufficient differential stress to initiate shear dilatancy. The decrease in permeability and pore volume is associated with compaction-dominated deformation.
4. The differences in the mechanical and transport properties of the two sandstones in response to cyclic stress are found to be correlated with their grain size distribution and grain morphology.

Appendix A

Grain Analysis of Castlegate and St Bees Sandstone

Variations in the Orientation of Sandstone Grains

Before cyclic loading experiments, Castlegate Sandstone, characterized by large grain size and high sphericity, displayed a wide distribution of Orientation Phi with no preferred direction. However, grains tend to align closer to directions perpendicular to the reference plane, with Orientation Theta slightly inclined towards 0° to 10°. After cyclic loading tests, a marked concentration of grains towards the Orientation Phi direction perpendicular to the reference plane is observed. Concurrently, the distribution of Orientation Theta (Fig. 18) also shows significant clustering towards the ranges of 0–10° and 80–90°. This indicates that grains are more likely to align within specific planes after cyclic loading, likely related to rotation and rearrangement under external forces. As confining pressure increased to 19.5 MPa, CG-3 displays less orientation concentration after cyclic loading. This reduction is likely due to increased friction between grains, which prevents grains from sliding and rearrangement (Fig. 18b, d). Under a confining pressure of 10.5 MPa and following cyclic loading, ST-2 sandstone exhibits a concentration of Orientation Phi below 10°, typically clustering around 90°. At the same time, the distribution of Orientation Theta became more dispersed. This

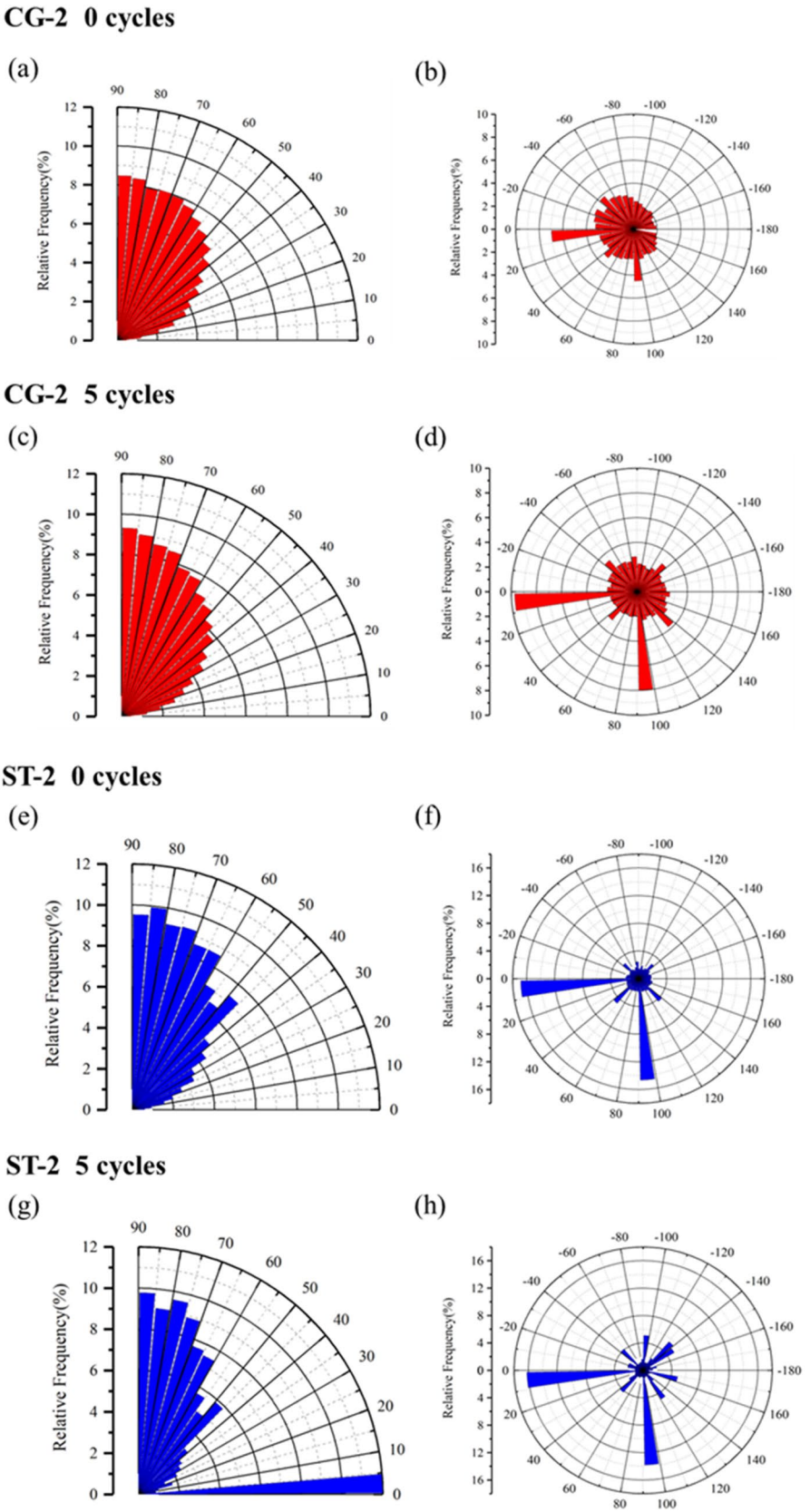

Fig. 18 Grain orientation before and after cyclic loading. The Phi orientation of the sandstone grain is between [0, + 90] degrees and the Theta direction of the grain is between [−180–180°]. Both are calculated by using the moment of inertia. For conciseness, only the data for CG-2 and ST-2 are included here

phenomenon is possibly due to the formation of new, smaller grains resulting from grain breakage. As the confining pressure reach 19.5 MPa, ST-3 sandstone exhibits a grain orientation distribution similar to that of Castlegate Sandstone following cyclic loading. Both Orientation Phi and Orientation Theta become concentrated in particular directions, suggesting a tendency for grain alignment and rotation along specific orientations in response to external forces.

Variations in Grain Size and Morphological Characteristics Before and After Cyclic Loading

Figure 19 illustrates that prior to the cyclic loading experiments, the grain size frequency histogram of Castlegate Sandstone exhibits a bimodal skewed distribution, with a majority of particles ranging in diameter from 175 to 375 μm, alongside a significant proportion of particles with diameters below 75 μm. Castlegate Sandstone showed a larger mean particle size and a wider range of particle size distribution compared to St Bees Sandstone. The latter displays a notably skewed grain size distribution, predominantly concentrated around 150 μm. Moreover, the roundness of grains in Castlegate Sandstone exceed that of St Bees Sandstone. After cyclic loading, Castlegate Sandstone displays comparable trends in grain size and grain shape alterations under varying confining pressure conditions. Specifically, these trends include a reduction in grain size peak and average grain size, albeit with no significant increase in overall grain counts (Fig. 19). Additionally, changes in grain shape are minimal (Figs. 19, 20), with sphericity and aspect ratio exhibiting negligible variations pre- and post-loading. Considering the changes in grain orientation before and after loading, see above, it is not difficult to conclude that the microstructural changes of Castlegate Sandstone under cyclic loading conditions are dominated by grain rearrangement (Fossen 2016; Lander and Walderhaug 1999; Luhmann et al. 2013; Rice-Birchall et al. 2022). In contrast, grain size and grain shape alterations in St Bees Sandstone before and after cyclic loading varied under different confining pressures. At 10.5 MPa confining pressure, ST-2 exhibited a noticeable decrease in particle size after cyclic loading, accompanied by a decrease in the proportion of grains with diameter > 350 μm and an increase in grains < 50 μm. Moreover, there was a significant increase in grain count after cyclic loading, alongside an increase in aspect ratio and a decrease in sphericity. Combined with the CT images, it is evident that strain localisation occurs within ST-2 sandstone under cyclic loading conditions, characterized by shear bands formed by fragmented grains. The newly formed fractured grains altered both the original grain morphology and the grain size distribution (Alikarami et al. 2015; Cheung et al. 2012). The change in its microstructure is predominantly governed by grain cracking (Wong and Baud 2012). However, there are less apparent variations in grain size and morphology within the ST-3 sandstone, showing a trend similar to the grain size and morphology before and after loading in Castlegate Sandstone. This suggests that microstructural alterations are primarily influenced by grain sliding and rearrangement rather than grain cracking.

According to previous studies, it is evident that local porosity and grain size distribution play pivotal roles in governing strain localisation within porous sandstone (Alikarami et al. 2015; Baud et al. 2017). Under the same stress path, Castlegate, characterised by a larger average grain size and broader grain distribution, demonstrates a higher local strength (Cheung et al. 2012). This phenomenon arises from the presence of smaller grains filling the interstices within larger grains, thereby impeding the propagation of damage, and exerting a significant mechanical influence. Consequently, under a confining pressure of 10.5 MPa, there is a lack of significant stress localisation within CG-2 sandstone, whereas shear bands developed within ST-2 sandstone. As the confining pressure increases to 19.5 MPa, the overall strength of ST-3 sandstone increases, thus preventing the formation of shear bands composed of fractured grains.

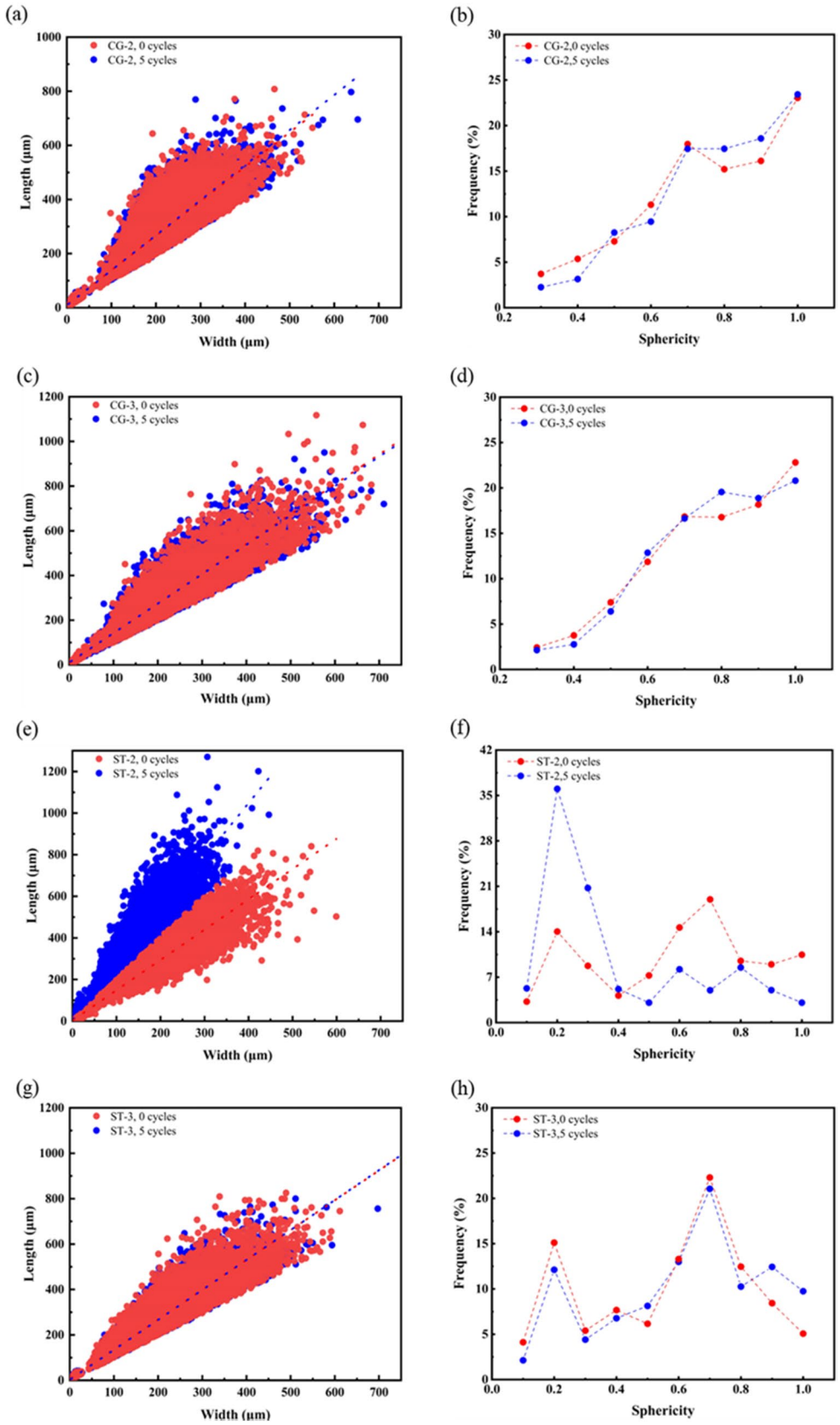

Fig. 19 The correlation between the length and width of the grains and the change in their sphericity before and after cyclic loading

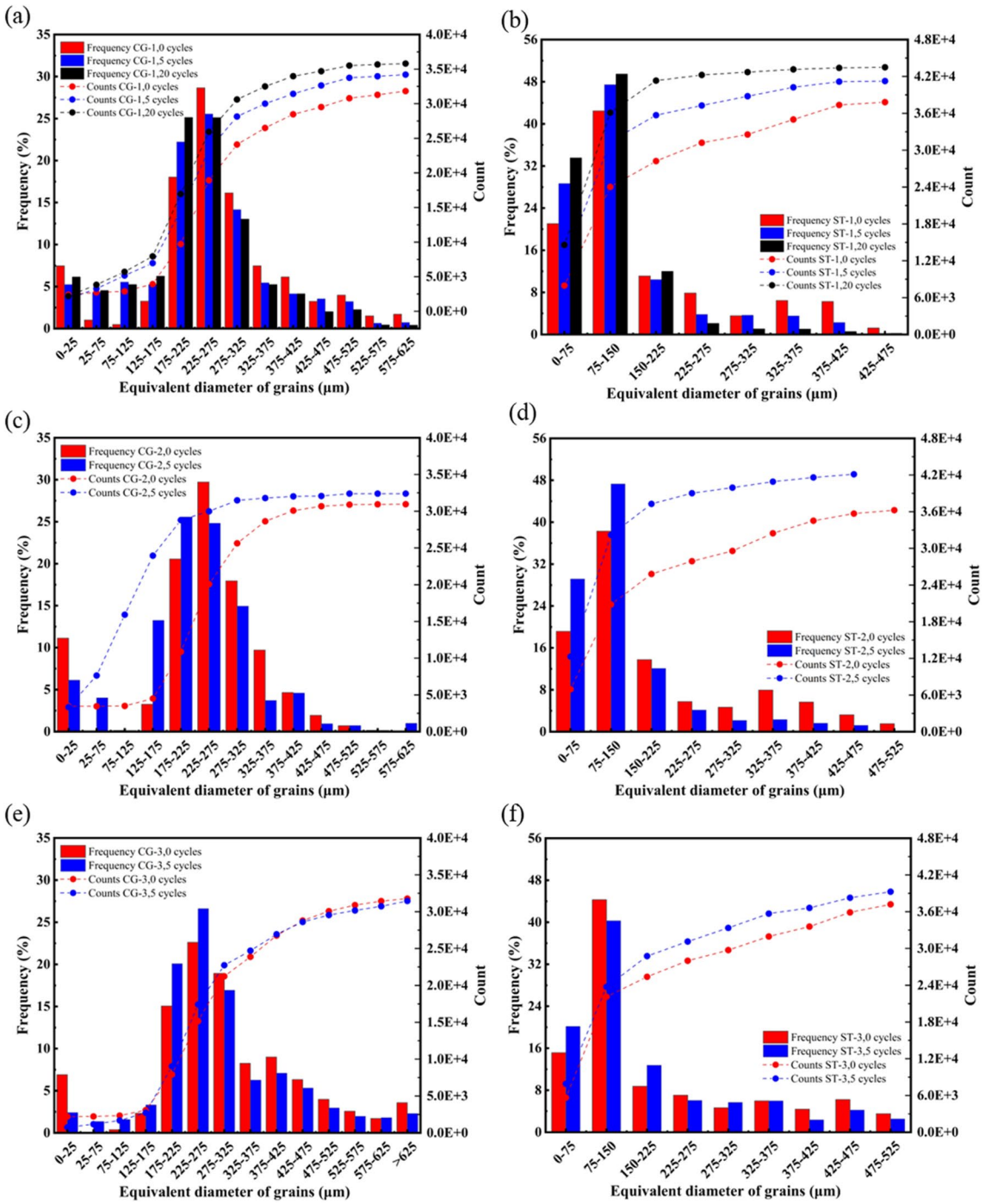

Fig. 20 Grain size distribution of Castlegate and St Bees sandstones before and after cyclic loading tests

Acknowledgements We would like to express our gratitude to the James Watt Scholarship from EGIS at Heriot-Watt University for its funding support, and to Jack Irvine for his great help in making the Harper's THMC Flow Workbench operational. Also, we sincerely thank the two anonymous reviewers for their valuable comments and constructive suggestions, which have significantly improved the quality of this paper.

Author Contributions Ming Wen: Conceptualization; Data curation; Methodology; Visualization; Writing–original draft; Writing–review & editing. Nick Harpers: Data curation; Methodology; Writing–original draft; Writing–review & editing. Nathaniel Forbes Inskip: Data curation; Methodology; Writing–review & editing. Jim Buckman: Data curation; Visualization; Writing–review & editing. Kamaljit Singh: Visualization; Writing–review & editing. Paul Miller: Data curation;

Writing–review & editing. Andreas Busch: Conceptualization; Supervision; Writing–original draft; Writing–review & editing.

Funding Not applicable.

Data availability The data that support the findings of this study are available within the article.

Declarations

Conflict of Interest The authors have no conflicts to disclose.

References

Alam AKMB, Niioka M, Fujii Y, Fukuda D, Kodama J-I (2014) Effects of confining pressure on the permeability of three rock types under compression. Int J Rock Mech Min Sci 65:49–61

Alikarami R, Andò E, Gkiousas-Kapnisis M, Torabi A, Viggiani G (2015) Strain localisation and grain breakage in sand under shearing at high mean stress: insights from in situ X-ray tomography. Acta Geotech 10:15–30

Baker R (2004) Nonlinear Mohr envelopes based on triaxial data. J Geotech Geoenviron Eng 130(5):498–506

Baud P, Exner U, Lommatzsch M, Reuschlé T, Wong, T.f. (2017) Mechanical behavior, failure mode, and transport properties in a porous carbonate. J Geophys Res 122(9):7363–7387

Bernabé Y, Li M, Tang Y-B, Evans B (2016) Pore space connectivity and the transport properties of rocks. Oil Gas Sci Technol 71(4):50

Canadell, J.G. et al., 2023. Intergovernmental Panel on Climate Change (IPCC). Global carbon and other biogeochemical cycles and feedbacks, Climate change 2021: The physical science basis. Contribution of working group I to the sixth assessment report of the intergovernmental panel on climate change. Cambridge University Press, pp. 673–816.

Carden P, Paterson L (1979) Physical, chemical and energy aspects of underground hydrogen storage. Int J Hydrogen Energy 4(6):559–569

Chen, W.-F. and Mizuno, E., 1990. Nonlinear analysis in soil mechanics. Elsevier Amsterdam.

Cheung, C.S., Baud, P. and Wong, T.f., 2012. Effect of grain size distribution on the development of compaction localization in porous sandstone. Geophysical Research Letters, 39(21).

David C, Darot M, Jeannette D (1993) Pore structures and transport properties of sandstone. Transp Porous Media 11:161–177

David C, Wong T-F, Zhu W, Zhang J (1994) Laboratory measurement of compaction-induced permeability change in porous rocks: Implications for the generation and maintenance of pore pressure excess in the crust. Pure Appl Geophys 143(1–3):425–456

Desbois G et al (2016) Multi-scale analysis of porosity in diagenetically altered reservoir sandstone from the Permian Rotliegend (Germany). J Petrol Sci Eng 140:128–148

Dong H, Blunt MJ (2009) Pore-network extraction from micro-computerized-tomography images. Phys Rev E 80(3):036307

Dong J-J et al (2010) Stress-dependence of the permeability and porosity of sandstone and shale from TCDP Hole-A. Int J Rock Mech Min Sci 47(7):1141–1157

Doyen PM (1988) Permeability, conductivity, and pore geometry of sandstone. J Geophys Res 93(B7):7729–7740

El Bied A, Sulem J, Martineau F (2002) Microstructure of shear zones in Fontainebleau sandstone. Int J Rock Mech Min Sci 39(7):917–932

Engeland K et al (2017) Space-time variability of climate variables and intermittent renewable electricity production–a review. Renew Sustain Energy Rev 79:600–617

Esterhuizen, G., Bajpayee, T., Ellenberger, J. and Murphy, M., 2013. Practical estimation of rock properties for modeling bedded coal mine strata using the Coal Mine Roof Rating, ARMA US Rock Mechanics/Geomechanics Symposium. ARMA, pp. ARMA-2013–154.

Fjaer E, Holt RM, Horsrud P, Raaen AM (2008) Petroleum related rock mechanics. Elsevier

Fossen H (2016) Structural geology. Cambridge University Press

Fowles J, Burley S (1994) Textural and permeability characteristics of faulted, high porosity sandstones. Mar Pet Geol 11(5):608–623

Fredrich J, Menéndez B, Wong T-F (1995) Imaging the pore structure of geomaterials. Science 268(5208):276–279

Gong L, Nie L, Xu Y (2020) Geometrical and topological analysis of pore space in sandstones based on X-ray computed tomography. Energies 13(15):3774

Gowd T, Rummel F (1980) Effect of confining pressure on the fracture behaviour of a porous rock. Int J Rock Mech Mining Sci Geomech Abstracts 17:225–229

Harpers, N., Wen, M., Miller, P., Hangx, S. and Busch, A., 2023. The Harpers THMC flow bench: A triaxial multi-reactor setup for the investigation of long-term coupled thermo-hydro-mechanical-chemical fluid-rock interaction. Review of Scientific Instruments, 94(9).

Hawkins A, McConnell B (1991) Sandstones as geomaterials. Q J Eng GeolHydrogeol 24(1):135–142

Heinemann N et al (2021) Enabling large-scale hydrogen storage in porous media–the scientific challenges. Energy Environ Sci 14(2):853–864

Herlinger R Jr, Vidal AC (2022) X-ray μCt extracted pore attributes to predict and understand Sor using ensemble learning techniques in the Barra Velha Pre-salt carbonates, Santos Basin, Offshore Brazil. J Petrol Sci Eng 212:110282

Hettema M, Schutjens P, Verboom B, Gussinklo H (2000) Production-induced compaction of a sandstone reservoir: the strong influence of stress path. SPE Reservoir Eval Eng 3(04):342–347

Hu C, Jia Y, Duan Z (2022) Pore and permeability properties of reservoir sandstone under a uniaxial compression CT test. J Natural Gas Sci Eng 104:104666

Huang S, Wang J, Qiu Z, Kang K (2018) Effects of cyclic wetting-drying conditions on elastic modulus and compressive strength of sandstone and mudstone. Processes 6(12):234

Huang Z et al (2021) Effects of confining pressure on acoustic emission and failure characteristics of sandstone. Int J Min Sci Technol 31(5):963–974

Iglauer S (2022) Optimum geological storage depths for structural H2 geo-storage. J Petrol Sci Eng 212:109498

Jia C et al (2018) Characterization of the deformation behavior of fine-grained sandstone by triaxial cyclic loading. Constr Build Mater 162:113–123

Kibikas WM, Bauer SJ (2021) Mechanical response of castlegate sandstone under hydrostatic cyclic loading. Geofluids 2021:1–18
Kong L, Ostadhassan M, Li C, Tamimi N (2018) Pore characterization of 3D-printed gypsum rocks: a comprehensive approach. J Mater Sci 53(7):5063–5078
Kong L, Ostadhassan M, Hou X, Mann M, Li C (2019) Microstructure characteristics and fractal analysis of 3D-printed sandstone using micro-CT and SEM-EDS. J Petrol Sci Eng 175:1039–1048
Kranz RL (1980) The effects of confining pressure and stress difference on static fatigue of granite. J Geophys Res 85(B4):1854–1866
Kumar KR, Honorio H, Chandra D, Lesueur M, Hajibeygi H (2023) Comprehensive review of geomechanics of underground hydrogen storage in depleted reservoirs and salt caverns. J Energy Storage 73:108912
Lander RH, Walderhaug O (1999) Predicting porosity through simulating sandstone compaction and quartz cementation. AAPG Bull 83(3):433–449
Lankof L, Tarkowski R (2020) Assessment of the potential for underground hydrogen storage in bedded salt formation. Int J Hydrogen Energy 45(38):19479–19492
Lindquist WB, Venkatarangan A, Dunsmuir J, Wong, T.f. (2000) Pore and throat size distributions measured from synchrotron X-ray tomographic images of Fontainebleau sandstones. J Geophys Res 105(B9):21509–21527
Liu C, Yu B, Zhang D, Zhao H (2020) Experimental study on strain behavior and permeability evolution of sandstone under constant amplitude cyclic loading-unloading. Energy Sci Eng 8(2):452–465
Lothe A, Gabrielsen R, Hagen NB, Larsen B (2002) An experimental study of the texture of deformation bands: effects on the porosity and permeability of sandstones. Pet Geosci 8(3):195–207
Luhmann AJ et al (2013) Permeability reduction produced by grain reorganization and accumulation of exsolved CO2 during geologic carbon sequestration: A new CO2 trapping mechanism. Environ Sci Technol 47(1):242–251
Lund H, Salgi G (2009) The role of compressed air energy storage (CAES) in future sustainable energy systems. Energy Convers Manage 50(5):1172–1179
Lysyy M, Fernø M, Ersland G (2021) Seasonal hydrogen storage in a depleted oil and gas field. Int J Hydrogen Energy 46(49):25160–25174
Masch FD, Denny KJ (1966) Grain size distribution and its effect on the permeability of unconsolidated sands. Water Resour Res 2(4):665–677
McPherson M, Johnson N, Strubegger M (2018) The role of electricity storage and hydrogen technologies in enabling global low-carbon energy transitions. Appl Energy 216:649–661
Medici G, West L, Mountney N (2018) Characterization of a fluvial aquifer at a range of depths and scales the triassic st bees sandstone formation, Cumbria UK. Hydrogeol J 26(2):565–591
Miall AD, Arush M (2001) The castlegate sandstone of the book cliffs, utah: sequence stratigraphy, paleogeography, and tectonic controls. J Sediment Res 71(4):537–548
Mortazavi A, Atapour H (2018) An experimental study of stress changes induced by reservoir depletion under true triaxial stress loading conditions. J Petrol Sci Eng 171:1366–1377
Ngwenya, B.T., Kwon, O., Elphick, S.C. and Main, I.G., 2003. Permeability evolution during progressive development of deformation bands in porous sandstones. Journal of Geophysical Research: Solid Earth, 108(B7).
Papamichos, E. et al., 2023. Coupled mechanical and permeability model for grain crushing and pore collapse, ARMA US Rock Mechanics/Geomechanics Symposium. ARMA, pp. ARMA-2023–0718.
Paterson MS, Wong T-F (2005) Experimental rock deformation: the brittle field, 348. Springer
Payton RL, Chiarella D, Kingdon A (2022) The influence of grain shape and size on the relationship between porosity and permeability in sandstone: a digital approach. Sci Rep 12(1):7531
Peng J, Rong G, Cai M, Zhou C-B (2015) A model for characterizing crack closure effect of rocks. Eng Geol 189:48–57
Pfeiffer WT, Bauer S (2015) Subsurface porous media hydrogen storage – scenario development and simulation. Energy Procedia 76:565–572
Pijnenburg RPJ, Spiers CJ (2020) Microphysics of inelastic deformation in reservoir sandstones from the seismogenic center of the groningen gas field. Rock Mech Rock Eng 53(12):5301–5328
Pijnenburg R, Verberne B, Hangx S, Spiers C (2018) Deformation behavior of sandstones from the seismogenic Groningen gas field: role of inelastic versus elastic mechanisms. J Geophys Res 123(7):5532–5558
Pijnenburg RPJ, Verberne BA, Hangx SJT, Spiers CJ (2019) Inelastic deformation of the slochteren sandstone: stress-strain relations and implications for induced seismicity in the groningen gas field. J Geophys Res 124(5):5254–5282
Popp T, Kern H, Schulze O (2001) Evolution of dilatancy and permeability in rock salt during hydrostatic compaction and triaxial deformation. J Geophys Res 106(B3):4061–4078
Rafieepour S et al (2021) Experimental investigation of depletion- and injection-induced changes in poromechanical, transport, and strength properties of high-porosity sandstone. SPE J 26(05):2793–2813
Rafieepour, S. et al., 2017. Experimental study of reservoir stress path and hysteresis during depletion and injection under different deformational conditions, ARMA US Rock Mechanics/Geomechanics Symposium. ARMA, pp. ARMA-2017–0416.
Ramezanian M, Emadi H (2020) Investigating effects of temperature and confining pressure on dynamic elastic properties and permeability—an experimental study. Geomech Energy Environ 22:100179
Reitenbach V, Ganzer L, Albrecht D, Hagemann B (2015) Influence of added hydrogen on underground gas storage: a review of key issues. Environ Earth Sci 73:6927–6937
Rice-Birchall E, Faulkner DR, Bedford JD (2022) The effect of grain size and porosity on the nature of compaction localisation in high-porosity sandstone. J Struct Geol 164:104740
Scholtès L, Donzé F-V (2013) A DEM model for soft and hard rocks: role of grain interlocking on strength. J Mech Phys Solids 61(2):352–369
Shalev E, Lyakhovsky V, Ougier-Simonin A, Hamiel Y, Zhu W (2014) Inelastic compaction, dilation and hysteresis of sandstones under hydrostatic conditions. Geophys J Int 197(2):920–925
Shirani Faradonbeh, R., Taheri, A. and Karakus, M., 2022. Fatigue failure characteristics of sandstone under different confining pressures. Rock Mechanics and Rock Engineering: 1–26.
Taheri A, Royle A, Yang Z, Zhao Y (2016) Study on variations of peak strength of a sandstone during cyclic loading. Geomech Geophysr Geo-Energy Geo-Resources 2(1):1–10
Teklu, T.W., Zhou, Z., Li, X. and Abass, H., 2016. Cyclic permeability and porosity hysteresis in mudrocks–experimental study, ARMA US Rock Mechanics/Geomechanics Symposium. ARMA, pp. ARMA-2016–108.
Vajdova, V., Baud, P. and Wong, T.f., 2004. Permeability evolution during localized deformation in Bentheim sandstone. Journal of Geophysical Research: Solid Earth, 109(B10).
Van den Hoek P et al (2000) A new concept of sand production prediction: theory and laboratory experiments. SPE Drill Complet 15(04):261–273
Wang H, Xu W, Cai M, Xiang Z, Kong Q (2017) Gas permeability and porosity evolution of a porous sandstone under repeated loading and unloading conditions. Rock Mech Rock Eng 50:2071–2083

Wong T, Baud P (1999) Mechanical compaction of porous sandstone. Oil Gas Sci Technol 54(6):715–727

Wong T-F, Baud P (2012) The brittle-ductile transition in porous rock: a review. J Struct Geol 44:25–53

Wong T-F, Zhu W (1999) Brittle faulting and permeability evolution: Hydromechanical measurement, microstructural observation, and network modeling. Geophys Monogr Ser 113:83–99

Wong, T.f., David, C. and Zhu, W. (1997) The transition from brittle faulting to cataclastic flow in porous sandstones: mechanical deformation. J Geophys Res 102(B2):3009–3025

Yang Y et al (2016) Influence of stress sensitivity on microscopic pore structure and fluid flow in porous media. Journal of Natural Gas Science and Engineering 36:20–31

Yang, X.-B., Han, X.-X., Wang, X.-Y. and Zhang, Z.-P., 2019. Effects of Constant Amplitude Cyclic Loading on the Nonuniform Deformation of Sandstone Specimens. Advances in Civil Engineering, 2019.

Zhang Z-H, Tang C-A (2020) A novel method for determining the crack closure stress of brittle rocks subjected to compression. Rock Mech Rock Eng 53(9):4279–4287

Zhang H, Wang L, Li J, Deng H, Xu X (2023) Study on the mechanical properties of unloading damaged sandstone under cyclic loading and unloading. Sci Rep 13(1):7370

Zhao Y, Zhou H, Zhong J, Liu D (2019) Study on the relation between damage and permeability of sandstone at depth under cyclic loading. Int J Coal Sci Technol 6(4):479–492

Zhou Z et al (2017) Influence of cyclic wetting and drying on physical and dynamic compressive properties of sandstone. Eng Geol 220:1–12

Zhu W, Wong TF (1996) Permeability reduction in a dilating rock: Network modeling of damage and tortuosity. Geophys Res Lett 23(22):3099–3102

Zhu W, Wong TF (1997) The transition from brittle faulting to cataclastic flow: Permeability evolution. J Geophys Res 102(B2):3027–3041

Zivar D, Kumar S, Foroozesh J (2021) Underground hydrogen storage: a comprehensive review. Int J Hydrogen Energy 46(45):23436–23462

Zoback MD (2010) Reservoir geomechanics. Cambridge University Press